Automatic Volcanic Ash Detection from MODIS Observations using a Back-Propagation Neural Network

By

Tami Gray

Thesis

Submitted to the Faculty of the

Graduate School of Vanderbilt University

in partial fulfillment of the requirements

for the degree of

MASTER OF SCIENCE

in

Earth and Environmental Sciences

May, 2015

Nashville, Tennessee

Approved:

Ralf Bennartz, Ph.D.

David Jon Furbish, Ph.D.

I dedicate this thesis to
my wonderful, generous, and most loving parents,
Tommy and Sissy Gray.

ACKNOWLEDGEMENTS

Above all, I would like to thank my Lord God, for all His guidance, patience, and unconditional love.

I must also thank my advisor, Dr. Ralf Bennartz, for his support, patience, instruction, and understanding. Thank you for pushing me to keep exploring and inspiring me to look at things from a different perspective!

I need to also thank Dr. John Rausch, for never turning me down when I desperately needed help with IDL.

Thank you to my colleagues in the Earth and Environmental Science Department at Vanderbilt for guidance, perspective, laughter when much needed, and above all, friendship. The relationships I have built with these people have made coming to school everyday a blessing and a joy.

Thanks, mom and dad, for always supporting me, encouraging me, and believing in me. It is truly a blessing to have you both. I love you!

I would also like to thank Dr. Mike Pavolonis of NOAA for helpful scientific discussions.

TABLE OF CONTENTS

LIST OF FIGURES

LIST OF TABLES

CHAPTER 1

INTRODUCTION

Volcanic eruptions, if large enough, can have a dramatic effect on the climate and the aviation industry, as highly explosive eruptions can emit large amounts of ash and SO_2 into the troposphere and stratosphere. Through the release of volcanic ash and SO_2, eruptions can act to cool Earth's climate (Kravitz, 2011), increase marine primary production (Langmann, 2014), disrupt precipitation patterns (Oman et al., 2006), and can have many other climate impacts, as discussed in Chapters 2.1-2.5. Climate effects of these eruptions are highly dependent on the location of the eruption (Schneider et al., 2009). For example, high-latitude eruptions can decrease the temperature gradient between Asia and Europe (Oman et al., 2006), whereas tropical eruptions have a winter warming effect over Northern Hemisphere continents (Robock et al., 1992). Volcanic ash can also have a significant impact on the aviation industry, as ash can lead to jet engine failure if injected into the aircraft (Sears et al., 2013), discussed in further detail in Chapter 2.6.

Due to these climate and aviation impacts, the knowledge of the location of volcanic ash following an eruption is imperative. This study aimed to explore the accuracy and reliability of using satellite observations to detect both ash-rich and SO_2-rich volcanic clouds using the Moderate Resolution Imaging Spectrometer (MODIS), an instrument on-board NASA's Terra and Aqua satellites, as discussed in Chapter 3. This thesis outlines chosen study areas in Chapter 3.2, remote sensing methods used to locate volcanic ash and SO_2-rich ash in MODIS observations in Chapter 3.3, modeling methods used to determine ash concentrations in Chapter 3.4, back-propagation neural networks in

Chapter 3.5, and the specific neural network training used for this study in Chapter 3.6. Optimal thresholds for detecting ash are discussed in Chapter 4.1. These thresholds were used to differentiate ash and SO_2-rich ash from ambient features, as detailed in Chapters 4.2. The results of this study can be found in Chapter 5.

CHAPTER 2

IMPACTS OF ERUPTIONS

2.1 Climate effects of volcanic ash

Although climate effects of eruptions have been mostly attributed to sulfate aerosols, recent research has attempted to quantify climate effects attributable to ash (Langmann, 2014; Flanner et al., 2014) (Figure 1).

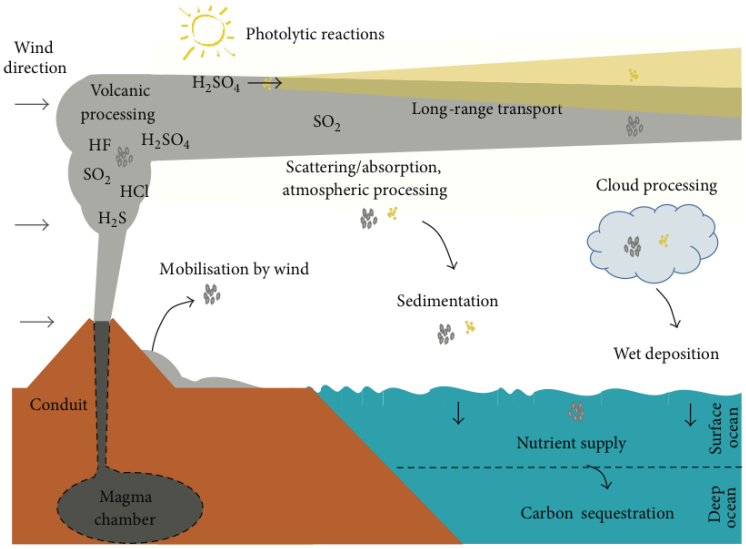

Figure 1: Diagram from Langmann, 2014, depicting the transport processes of dust (yellow) and volcanic ash (gray), radiative effects, cloud processes, deposition, and ocean fertilization.

Volcanic ash acts to reduce the amount of incoming solar radiation, thus modifying Earth's surface temperature (Langmann, 2013). Ash, in addition to sulfate aerosols, provides a source of cloud condensation nuclei and ice nuclei, increasing the number of cloud droplets (Langmann, 2014; Langmann, 2013; Twomey, 1977). An increase in cloud droplets, or the first indirect effect, modifies cloud lifetime and precipitation processes, otherwise known as at the second indirect effect (Langmann, 2014; Langmann,

2013; Albrecht, 1989). Atmospheric CO_2 concentrations can be reduced following volcanic eruptions through ocean fertilization: Ash serves as a source of iron to the ocean, increasing marine primary production, leading to a build-up of organic carbon (Langmann, 2014; Langmann, 2013; Achterberg et al., 2013). Radiative forcing associated with ash is largely dependent on the reflective properties of the surface it is over (Flanner et al., 2014). Following the eruption of Ejyafjallajokull in 2010, a positive radiative forcing, or an increase in Earth's energy budget, was found when ash was deposited onto snow and ice (Flanner et al., 2014). In addition to modification to radiative forcing, ash can result in surface darkening, snow melt, and snow insulation (when the ash deposit is thick) (Flanner et al., 2014). Although sulfate aerosols provide a larger contribution to negative radiative forcing, sulfate concentrations can vary from large to small with each eruption. During Ejyafjallajokull, little SO_2 was injected into the atmosphere, and thus long-wave positive radiative forcing was much larger than long-wave forcing associated with sulfate (Flanner et al., 2014.)

2. 2 Climate effects of sulfate aerosols

In order to have a significant climate effect, sulfate aerosols must be injected into the stratosphere because they will be rapidly removed due to precipitation if only injected into the troposphere (Francis and Oppenheimer, 2004). Sulfate aerosols, formed after SO_2 oxidizes to H_2S0_4 by homogeneous nucleation/condensation onto other aerosols (Vernier et al., 2011), increase Earth's albedo by scattering shortwave radiation (Figure 1). This results in the primary effect of large volcanic eruptions: surface and tropospheric cooling and stratospheric warming (Kravitz, 2011). If only injected into the troposphere, sulfate

aerosols will have a lifetime of 1-3 weeks due to precipitation. Once injected into the stratosphere their lifetime increases to 1-3 years, resulting in reduction of direct solar flux at the surface and net cooling. Net heating is observed in the stratosphere due to the absorption of infrared radiation by sulfate aerosol. Other effects of sulfate aerosols are ozone depletion and more downward infrared flux (Robock, 2000).

Due to synoptic-scale weather systems, radiation-gain differences and global atmospheric circulation patterns, climate implications of volcanoes will depend on where and when they erupt. When injected at high latitudes, sulfate aerosols have a lifetime of one year or less due to subsidence over the poles (Oman et al., 2005). If injected at low-latitudes, sulfate aerosols will have a longer lifetime: 1-3 years (Kravitz, 2011). Both tropical and high-latitude eruptions lead to continental cooling during summer, enhanced cooling over regions already characterized by sea-ice during the winter in the Northern Hemisphere, and a decrease in global precipitation (Schneider et al., 2009).

2.3 Seasonal effects of low-latitude eruptions

Climate models indicate the primary effects of large tropical eruptions to be winter warming over the Northern Hemisphere continents (Robock et al., 1992) and a positive Arctic Oscillation (Kravitz, 2011), a phase characterized by low pressure over the Arctic and high pressure over the mid-latitudes. A strengthening of the Polar Vortex, a result of an increased temperature gradient between the Equator and the poles following stratospheric warming, forces a positive Arctic Oscillation and keeps cold air locked at the poles. Following the tropical eruption of Pinatubo in 1991, ozone levels were reduced by 6-8%, winter warming was observed in 1993, summer cooling was observed in 1993,

a decrease in solar flux, the amount of radiation not being scattered (NOAA), was observed, and an increase in diffuse flux, the amount of radiation reaching the surface that has been scattered (NOAA), was observed (Francis and Oppenheimer, 2004).

2.4 Seasonal effects of high-latitude eruptions

Although tropical eruptions are thought to have a more significant climate impact than high-latitude eruptions, a large enough high-latitude eruption, erupting at the right time of year with significant SO_2, could have a dramatic effect on climate, especially with regard to monsoonal regions. Following high-latitude eruptions, a reduced temperature gradient between Asia and Europe leads to the weakening of the Indian and African monsoons (Oman et al., 2006), and thus significant warming is seen over the Sahel of Africa and the southern portion of the Arabian Peninsula and India due to a decrease in cloud cover and soil moisture (Graf, 1992). This combination of increased temperature and decreased cloud cover would enhance evaporation and thus reduction of river flows (Oman et al., 2006). For example, a reduction in the flow of the Nile has been

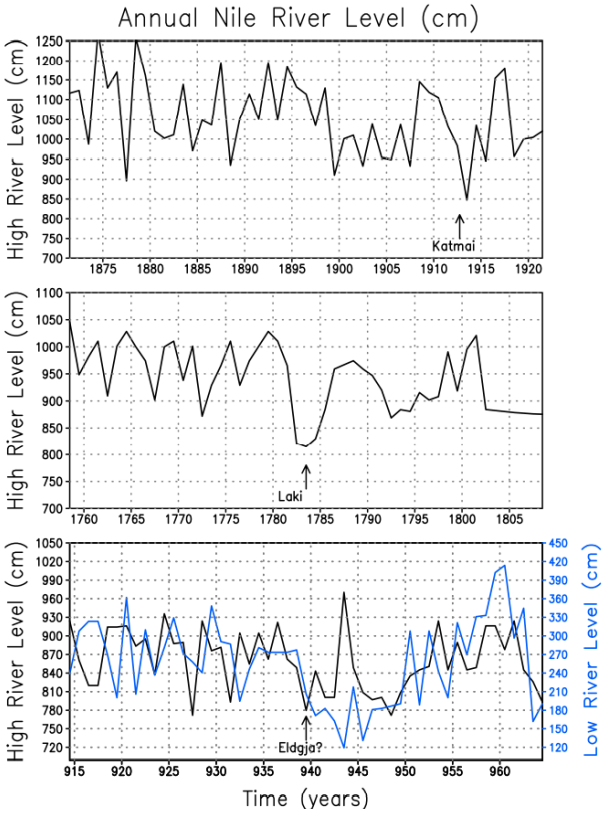

Figure 2: Reduction in Nile river levels as a result of precipitation reduction following three high-latitude volcanic eruptions (Oman et al., 2006): Top: Katmai, 1912; Middle: Laki, 1783-1784; Bottom: Eldgjá, 939

observed following high-latitude eruptions, such as Laki in Iceland in 1783- 1784, Katmai in 1912, and Eldgjá in 939 (Figure 2) (Oman et al., 2006).

2.5 Long-term effects of eruptions

In addition to the direct, seasonal effects of high and low-latitude eruptions, there are also positive feedbacks, or developments that enhance changes already occurring, that may lead to long-term climate change. In addition to winter warming of Northern Hemisphere continents, tropical eruptions also result in cooling of high-latitudes in the Northern Hemisphere, suggesting that there are multiple positive feedbacks in regions characterized by ice and snow with regard to further cooling (Schneider et al., 2009). The response to tropical eruptions is enhanced by advancing sea ice and lower sea surface temperatures, associated with a stronger temperature gradient between the Equator and poles at the surface. During Northern Hemisphere winter, the Arctic then cools much more quickly than the tropics, suggesting that volcanism might play a part in long-term climate change (Schneider et al., 2009).

2.6 Aviation threats

In addition to human health impacts, such as eye irritation and respiratory stress (Langmann, 2013), volcanic ash poses a serious threat to the aviation industry. Ash can melt onto the jet engine turbine and lead to failure if it enters the engine, as the melting point of ash is around 1100 K while jet engines operate at about 1400 K (Sears et al., 2013). In addition to engine damage, volcanic ash can also damage cockpit windows and other airplane surfaces through sandblasting, clog the pitot-static system, and be ingested

into the air conditioning and cooling systems (Pavolonis et al., 2013; International Civil Aviation Organization (ICAO), 2007). Due to these physical damage effects of volcanic ash, the presence of ash in the atmosphere can significantly effect the economy of the aviation industry. For example, the eruption of Eyjafjallajokull in Iceland in 2010 resulted in over 100,000 canceled flights (Pavolonis et al., 2013; International Civil Aviation Organization (ICAO), 2007). Just fewer than 100 aircraft have been damaged due to interaction with volcanic ash within 30 years (1970-2000) (Sears et al., 2013).

2.7 Trajectories of ash and SO_2

The location of ash and SO_2 following an eruption is important due to the resulting climate effects and aviation threats. However, ash and SO_2 often follow different trajectories due to their different densities and the presence of shear, or the change in wind speed and direction with height, and atmospheric lifetime (Carn et al., 2002; Sears et al., 2013; Schneider et al., 1999; Prata et al., 2007; Rose et al., 2000; Thomas et al., 2011). When this happens, SO_2 cannot reliably be used as a proxy for ash. *Sears et al.* [2013] found that sometimes only 10% of ash was missed when using SO_2 as a proxy for ash, but other times that over 80% was missed. They go on to discuss that although not always highly accurate, using SO_2 to determine the location of volcanic ash is useful.

CHAPTER 3

METHODS

3.1 Summary

To determine if volcanic ash could be automatically detected within MODIS observations, MODIS data was obtained for seven eruptive events (Table 1) and band differencing was performed to distinguish ash and SO_2-rich ash from ambient clouds and surface features. Ash concentrations were determined using HYSPLIT for the same eruptive events. The accuracy of using a neural network to detect volcanic ash was explored by training a back-propagation neural network with band differences representing ash, SO_2, and surface features as input and ash concentrations as output.

3.2 Study areas

Seven eruptive events with similar plume heights and explosivity were chosen (Table 1). These eruptions all had a Volcanic Explosivity Index (VEI) of 3 or 4 and plume heights between 12 and 30 km (*Global Volcanism Program;* hereafter referred to as GVP). The VEI is on a scale of 0 to 8, where an increase of one indicates an increase in magnitude by a factor of 10, and is a function of volume of erupted material, eruption column height, and duration (Newhall et al., 1982). These eruptive events were chosen because they had similar eruptive column heights, allowing their trajectories to be compared.

Volcano	Date of Eruption	Location	Plume Height (km)	VEI
Kasatochi	08/07/2008	52.177°N, 175.508°W	~19	4
Okmok	07/12/2008	53.43°N, 168.13°W	~15	4
Grímsvötn	05/21/2011	64.42°N, 17.33°W	~20	4
Chaitén	05/06/2008	42.833°S, 72.646°W	~30	4
Puyehue-Cordón Caulle	06/04/2011	40.59°S, 72.117°W	~12	3
Kelut	04/13/2014	7.93°S, 112.31°E	~17	4
Sangeang Api	05/30/2014	8.20°S, 119.07°E	~15	3

Table 1: Seven volcanic eruptions and their corresponding time, location, plume height (km), and explosivity.

Kasatochi, a stratovolcano located in the Aleutian Islands (Sigurdsson, 2000), began erupting on August 7, 2008, with three distinct pulses. The third pulse, beginning at 0435 UTC, August 8, 2008, was the largest of the three, with a plume height of 19 km (Pavolonis, personal comm.), and continued for 14 hours (Prata et al., 2010). This pulse released the most ash of the three pulses (Fee et al., 2010), and released around 1.7 Tg of SO_2 (Corradini et al., 2010), the highest amount observed since the eruption of Hudson in 1991 (Fee et al., 2010).

Another volcano located in the Aleutian Islands, the basaltic shield volcano Okmok, erupted at 1943 UTC on July 12, 2008 (Fee et al., 2010), with a plume height near 15 km (GVP). This phreatomagmatic eruption, or one characterized by high water content (Fee et al., 2010), released 0.1 Tg of SO_2 (Prata et al., 2010).

The eruption of Grímsvötn, a basaltic caldera (Sigurdsson, 2000) lying below the Vatnajökull icecap in Iceland (GVP), began erupting around 1900 UTC, May 21, 2011

(Petersen et al., 2012). The plume quickly reached 20 km (GVP), but decreased strength soon afterwards and the plume fell to 10 km within 24 hours (Petersen et al., 2012).

Chaitén, a rhyolitic caldera in southern Chile, began erupting on May 2, 2008 (Lara, 2009). This eruptive event continued for months, but on May 6, 2008, 12:32 UTC, produced the second Plinian column of the event with a plume height of over 20 km (Lara, 2009; GVP). This eruption is especially interesting as it was the first rhyolitic eruption during the satellite era (Lara, 2009). This eruption was not associated with high SO_2 emissions (Lara, 2009; Carn et al., 2009).

Also in Chile, Puyehue-Cordón Caulle, a volcanic complex, began erupting from a fissure on June 4, 2011 (GVP; Klüser et al., 2012; Sigurdsson, 2000). This basaltic-to-rhyolitic eruption continued for several months (Diaz et al., 2014), but initially sent ash 12 km into the atmosphere (GVP; Klüser et al., 2012). Within ten days, Puyehue's ash cloud had circled the globe (Klüser et al., 2012).

On February 13, 2014, 15:50 UTC, Kelut, a stratovolcano located in Java, began erupting. This eruption sent volcanic ash to altitudes of 17 km, continued for 3-4 days, and resulted in 40 canceled flights and multiple rerouted flights (GVP; Kristiansen et al., 2015). Kelut is estimated to have injected a total of 0.74 Tg of ash into the atmosphere, and 0.38 Tg of that ash into the stratosphere (Kristiansen et al., 2015).

Sangeang Api, a volcanic complex in the Lesser Sunda Islands (Sigurdsson, 2000), began erupting on May 30, 2014, 8:55 UTC (GVP). This trachybasaltic-to-trachyandesitic complex emitted ash up to 15.2 km and resulted in canceled flights from the Darwin International Airport (GVP).

3.3 Remote sensing

Aerosols exhibit varying transmittance in the 8-10 and 10-12 μm ranges, regions where the atmosphere is nearly transparent (Ackerman, 1997) (Figure 3). Because MODIS channels 29, 31, and 32 cover this spectral range, MODIS images were obtained and band combinations were derived to determine areas of ash and SO_2 in each eruptive column. Sulfur dioxide is very absorptive in 7.3 and 8.6 μm channels (Prata et al., 2007). However, the 7.3 μm channel is not as sensitive to the total SO_2 column as the 8.6 μm channel because the 7.3 μm channel lies within a band that is also sensitive to water vapor (Sears et al., 2013) (Figure 3).

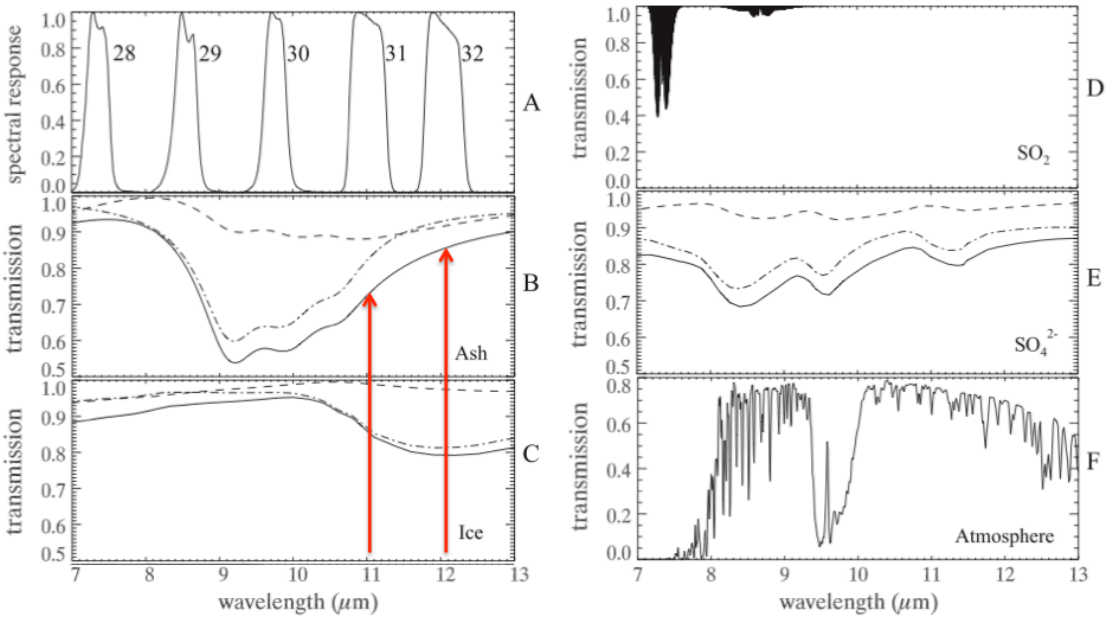

Figure 3: (A) Spectral response for MODIS channels 28, 29, 30, 31, and 32; (B) Ash transmission spectra; (C) Ice transmission spectra; (D) Strength of SO_2 absorption in channels 7.3 μm versus 8.6 μm; (E) Sulfate, water droplets transmission spectra; (F) Transmission spectra of the atmosphere. Figure adapted from *Watson et al., 2004*.

Band differencing was used to locate both ash and SO_2 in the atmosphere following a volcanic eruption. Ash is characterized by a negative brightness temperature difference

between 11 and 12 μm (Ackerman et al., 2008) (Figure 3). The brightness temperature is the equivalent blackbody temperature required to emit the same radiance observed by the satellite instruments in a particular channel (Bennartz, 2015). Ice is characterized by a positive brightness temperature difference between 11 and 12 μm because ice exhibits a lower brightness temperature at 12 μm (Watson et al., 2004). Band differencing was also used to determine ice loading within the volcanic clouds, as ice can affect the signal of ash and SO_2 within the cloud, leading to a misrepresentative loading of ash and SO_2 (Watson et al., 2004). Following methods similar to *Ackerman et al.* [2008], band 31 (11 μm) was subtracted from band 32 (12 μm) to create a positive brightness temperature difference representing ash. Because SO_2 absorbs strongly in the 8.6 μm channel but not in the 11 μm channel, band 29 (8.6 μm) was subtracted from band 31 (11 μm) to create a positive brightness temperature difference representing SO_2 (Figure 3). Visible images were also created for each case by combining band 1 (620-670 nm), band 4 (545-565 nm), and band 3 (459-479 nm) (Figure 4).

A

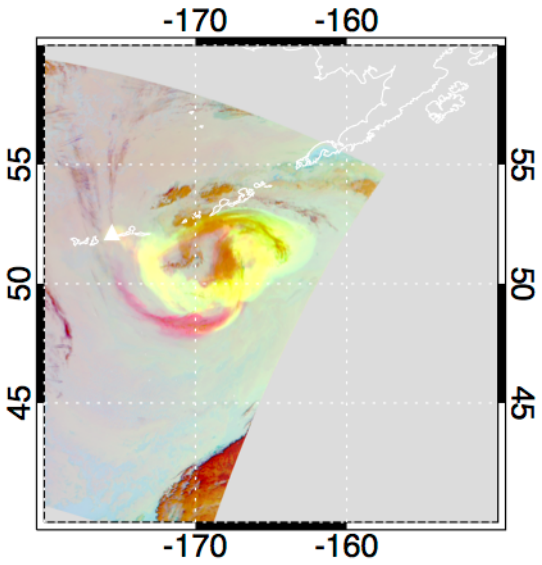
-170
-160
55
50
45

B

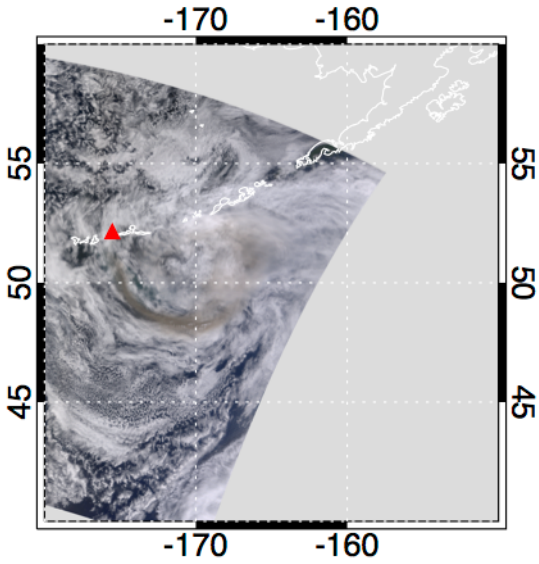
-170
-160
55
50
45

C

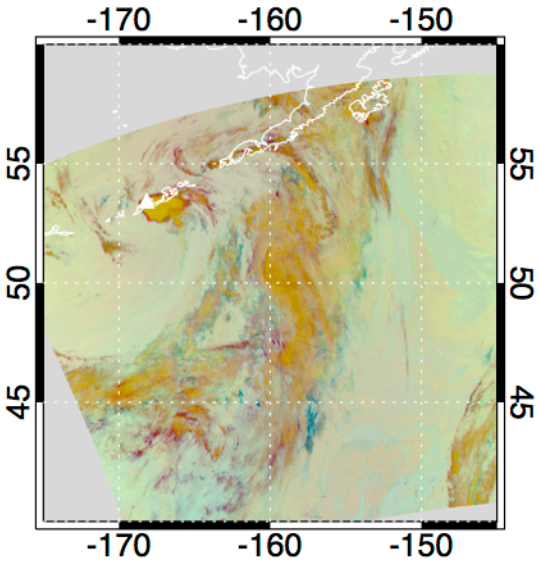
-170
-160
-150
55
50
45

D

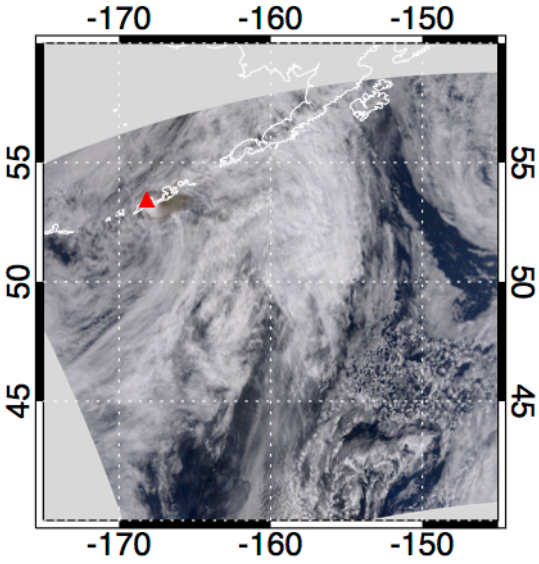
-170
-160
-150
55
50
45

E

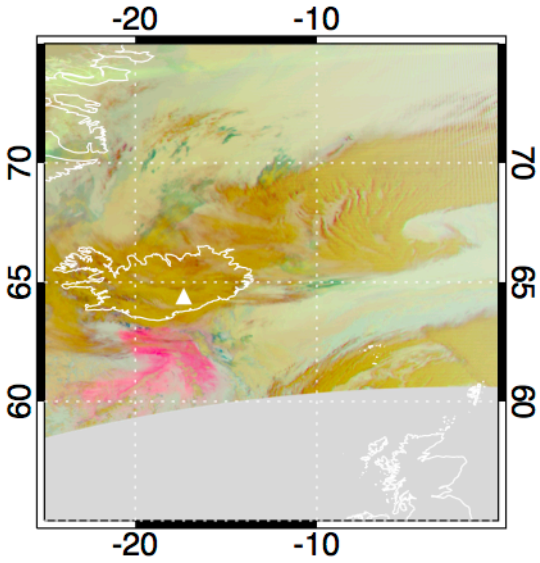

F

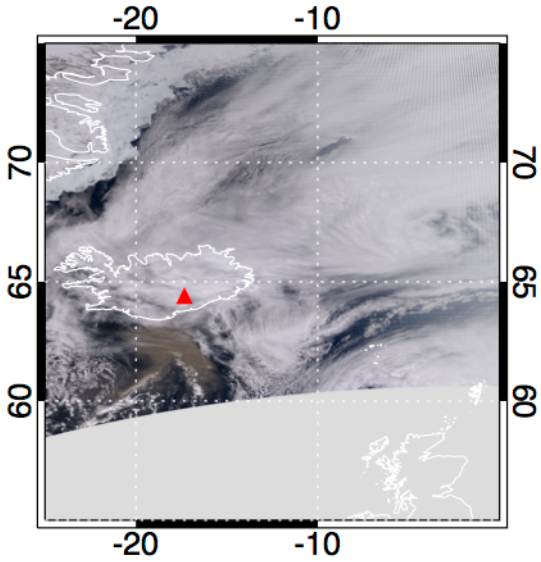

G

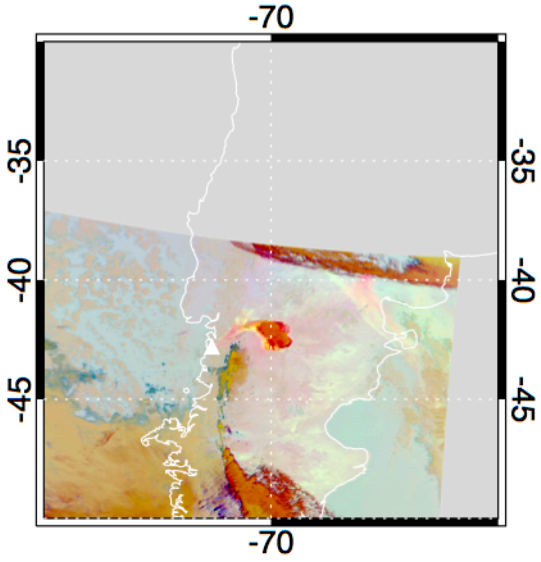

H

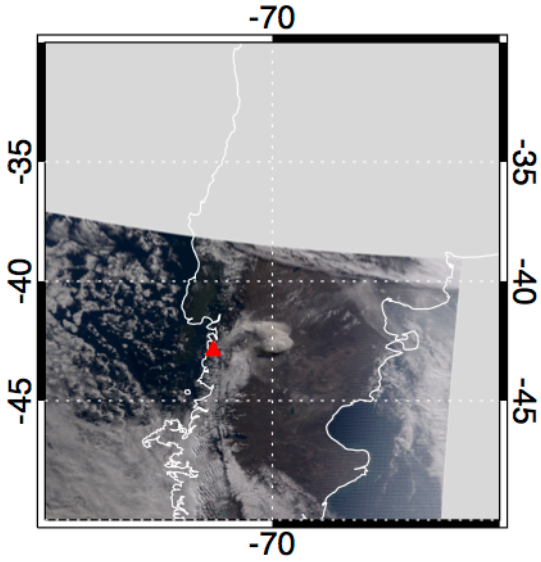

I

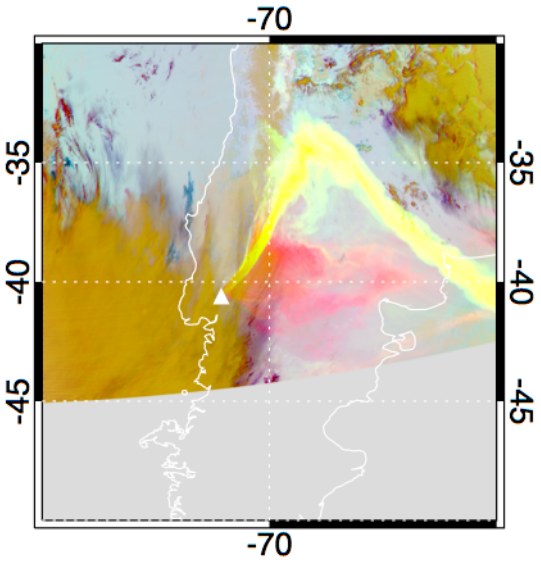
-70
-35
-40
-45
-70

J

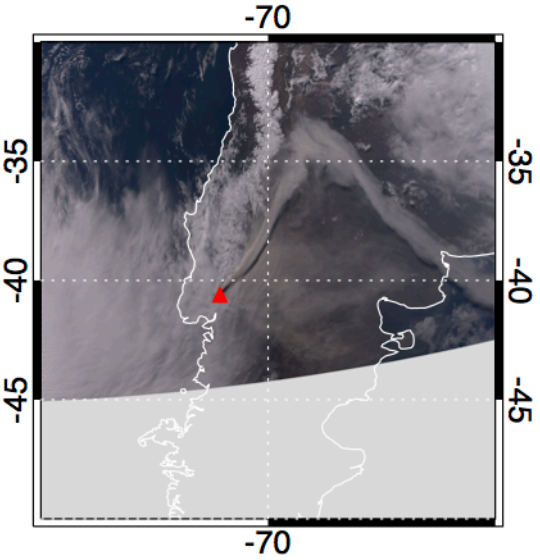
-70
-35
-40
-45
-70

K

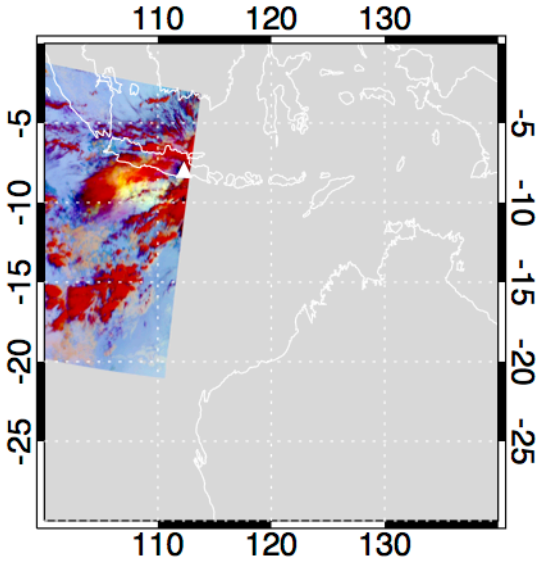
110
120
130
-5
-10
-15
-20
-25

L

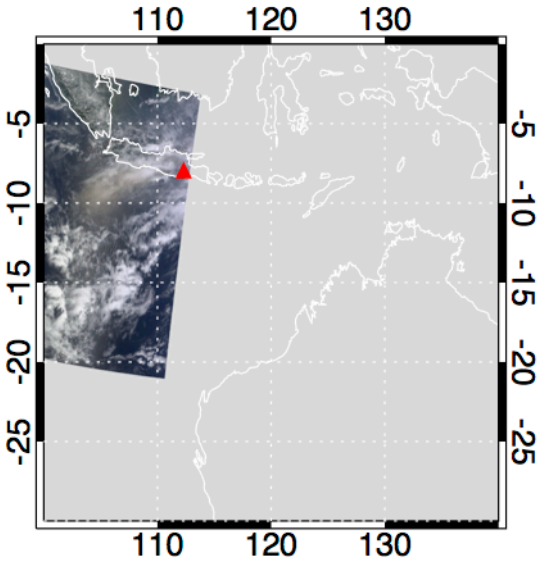
110
120
130
-5
-10
-15
-20
-25

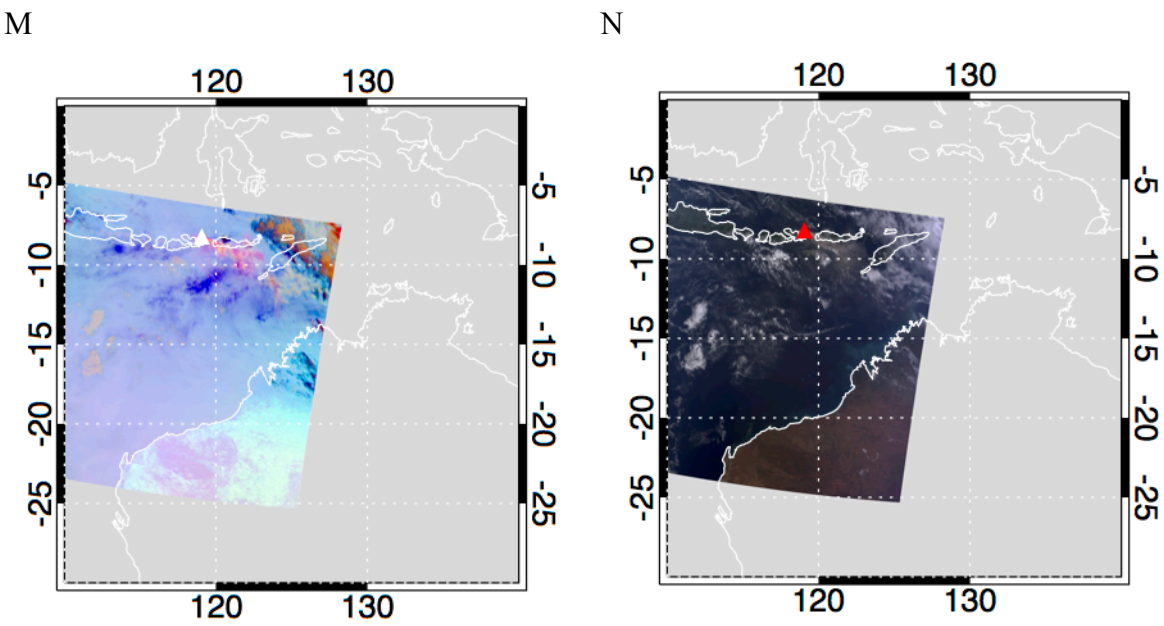

Figure 4: RGBs were created using MODIS bands 32-31, 31-29, and 31, for following eruptions and times: (A) Kasatochi, August 8, 2008, 2305Z; (C) Okmok, July 12, 2008, 2330Z; (E) Grímsvötn, May 23, 2011, 1400Z; (G) Chaitén, May 6, 2008, 1505Z; (I) Puyehue-Cordón Caulle, June 6, 2011, 1840Z; (K) Kelut, February 14, 2014, 0335Z; (M) Sangeang Api, May 31, 2014, 0235; Visible images were created for the same times to the right of their corresponding RGB using MODIS bands 1, 4, and 3: (B), (D), (F), (H), (J), (L), (N). Ash will appear brown in these images and meteorological clouds appear white.

Previous research determining locations and loadings of SO_2 and ash has used one or a combination of the following satellite instruments: Total Ozone Mapping Spectrometer (TOMS), Moderate Resolution Imaging Spectrometer (MODIS), Atmospheric Infrared Sounder (AIRS), Spinning Enhanced Visible and Infrared Imager (SEVIRI), Ozone Monitoring Instrument (OMI), and the Advanced Very High Resolution Radiometer (AVHRR) (Ackerman, 1997; Carn et al., 2009; Carn et al., 2010; Feltz et al., 2006; Prata et al., 2007; Prata et al., 2010; Theys et al., 2013; Pavolonis, 2014; Pavolonis et al., 2006).

3.4 HYSPLIT

After band combinations are used to differentiate between ambient clouds, surface features, ash, and SO_2, ash concentrations are determined using the Hybrid Single-Particle Lagrangian Integrated Trajectory (HYSPLIT) Model for Volcanic Ash for the same archived eruptions (Draxler and Rolph, 2003).

The NOAA/Air Resources Laboratory HYSPLIT model can be used specifically for archived volcanic eruptions to determine the transport, dispersion, and ash concentrations of the volcanic plume. For this particular study, National Centers for Environmental Prediction (NCEP)/National Center for Atmospheric Research (NCAR) Reanalysis meteorological data was used. Reanalysis data is composed of atmospheric analysis reproduced using historical data (1948-current) (Kalnay et al., 1996).

The following source term parameters were specified for each eruption (Appendix A): eruption starting time (UTC), latitude and longitude of volcano, ash column top, ash column bottom, eruption duration, and ash quantity. The ash column top was chosen to be the maximum plume height, as reported in the literature and weekly reports via GVP. The ash column bottom was always the volcano's summit height, and HYSPLIT evenly distributes emissions vertically between the top and bottom column heights (Draxler and Rolph, 2003). Eruption durations were chosen based on the nature of the eruption: single puff versus continuous release. Eruption ash quantities were chosen from published literature (Appendix A) unless unknown. When unknown, USGS Eruption Source Parameters, assignments of column height, duration, mass eruption rate, volume, and percentage of fine ash based on eruption type, were used for ash quantities (Mastin et al., 2009).

The following runtime parameters were also specified for each eruption (Appendix A): total duration, sampling type, average period/snapshot interval, concentration grid resolution (decimal degrees), concentration grid domain size (decimal degrees), top of layer, and bottom of layer. Simulations were run for either 24 or 48 hours, depending on the eruption. The sampling type and interval were chosen to be snapshot and three hours, respectively, for each eruption, resulting in output at a 3-hour interval. As HYSPLIT determines concentrations within a 3-dimensional latitude-longitude grid, the concentration grid resolution is the horizontal resolution and the concentration domain size is synonymous with horizontal dimensions. As noted in Appendix A, these grid and domain sizes are all "-1," which tells HYSPLIT to automatically calculate these sizes based on the total runtime (Draxler and Rolph, 2003). The simulation of the Chaitén eruption, which was run for 24 hours, had a resolution of 0.2 degrees, while all other eruptions, which were run for 48 hours, had resolutions of 0.4 degrees. To calculate the vertical layer-average concentration, HYSPLIT was given the upper and lower limits of atmospheric layer, with the lower limit set to mean sea level and the upper limit to 30 km for all eruptions except Chaitén, which had an ash column height very close to this upper limit. Because of this, Chaitén's upper limit was chosen to be 32 km, the most HYSPLIT could handle without crashing.

The following deposition/ashfall parameters were used: wet deposition of particle, in cloud and below cloud; the option to sum deposition over total run time; ash bulk density; and the option to specify output units. The wet deposition parameters were kept as default: In-cloud kept at 3.2E+05 liters/liters; Below-cloud was kept at 5.0E-05 liters^{-1}. Deposition was set to the sum over the entire run for each eruption. Ash bulk density and

deposition output units were both kept at default: 2.5 g/cm^3 and mass/area, respectively. Concentrations were output in kg/m^3 (Figure 5). These concentrations were converted to grams and integrated over the concentration layer height of 30 km or 32 km, depending on the eruption, resulting in units of g/m^2.

A

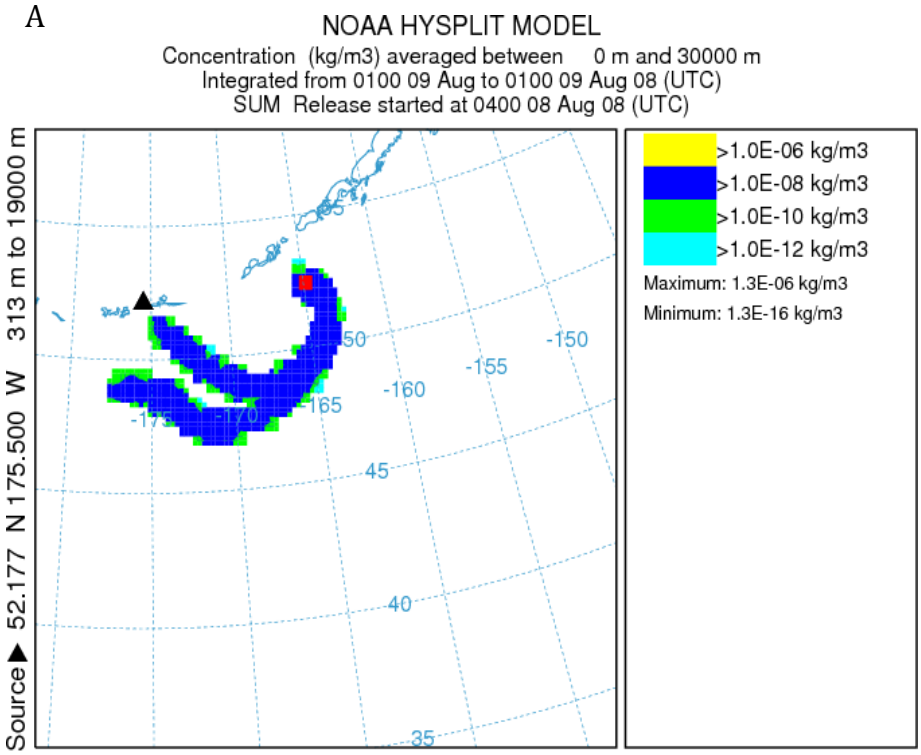

B

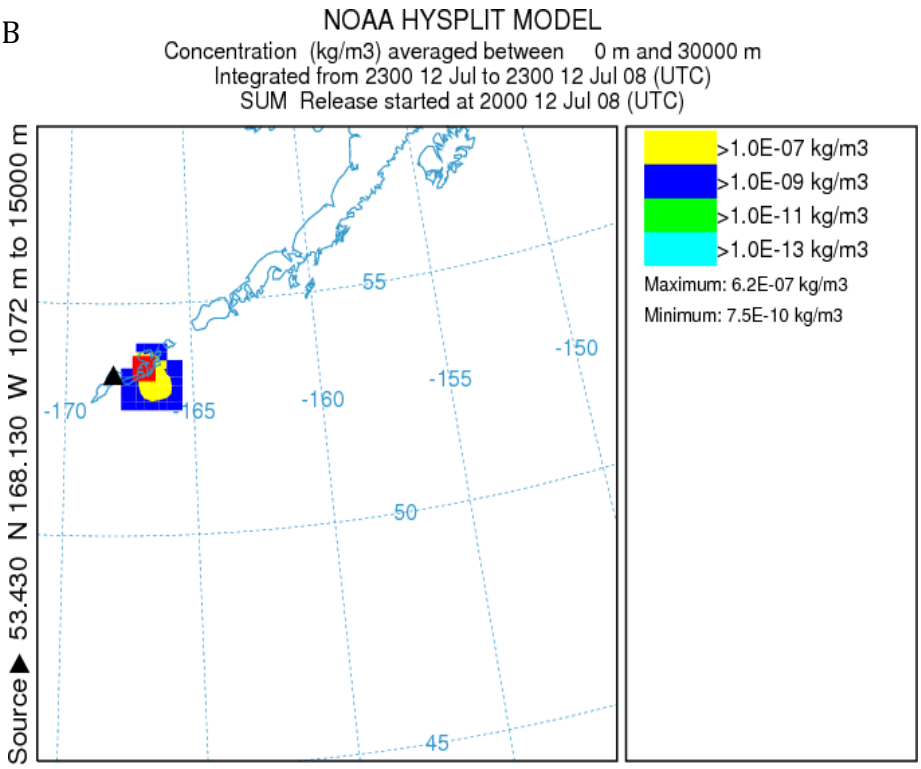
NOAA HYSPLIT MODEL
Concentration (kg/m3) averaged between 0 m and 30000 m
Integrated from 2300 12 Jul to 2300 12 Jul 08 (UTC)
SUM Release started at 2000 12 Jul 08 (UTC)
Source ▲ 53.430 N 168.130 W 1072 m to 15000 m
>1.0E-07 kg/m3
>1.0E-09 kg/m3
>1.0E-11 kg/m3
>1.0E-13 kg/m3
Maximum: 6.2E-07 kg/m3
Minimum: 7.5E-10 kg/m3
55
-150
-155
-160
-165
-170
50
45

C

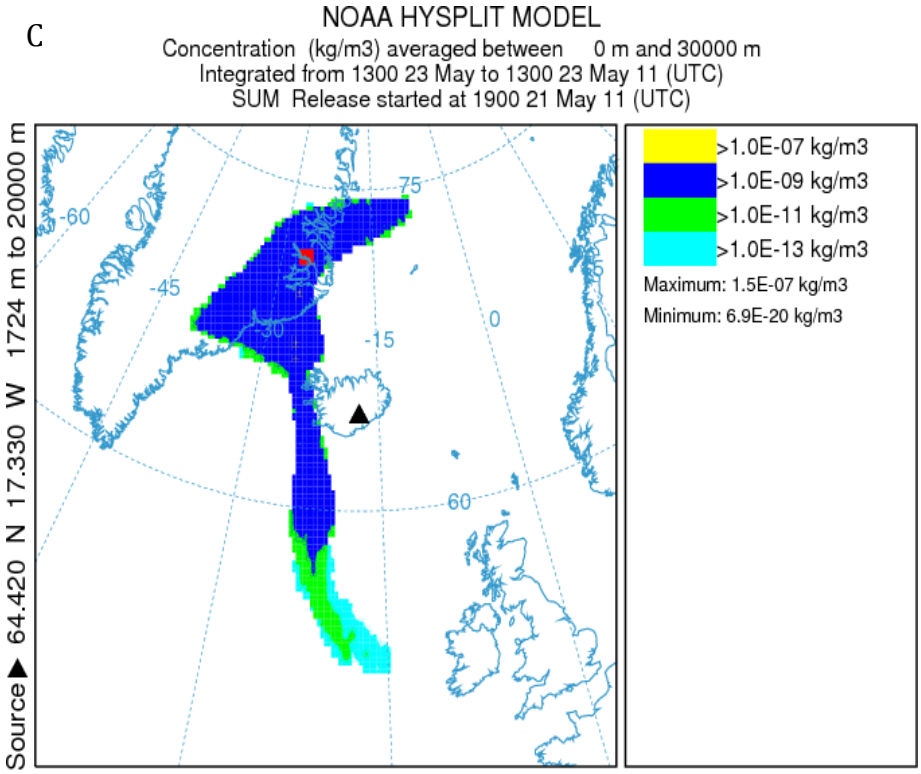
NOAA HYSPLIT MODEL
Concentration (kg/m3) averaged between 0 m and 30000 m
Integrated from 1300 23 May to 1300 23 May 11 (UTC)
SUM Release started at 1900 21 May 11 (UTC)
Source ▲ 64.420 N 17.330 W 1724 m to 20000 m
>1.0E-07 kg/m3
>1.0E-09 kg/m3
>1.0E-11 kg/m3
>1.0E-13 kg/m3
Maximum: 1.5E-07 kg/m3
Minimum: 6.9E-20 kg/m3
75
-60
-45
0
-15
60

D

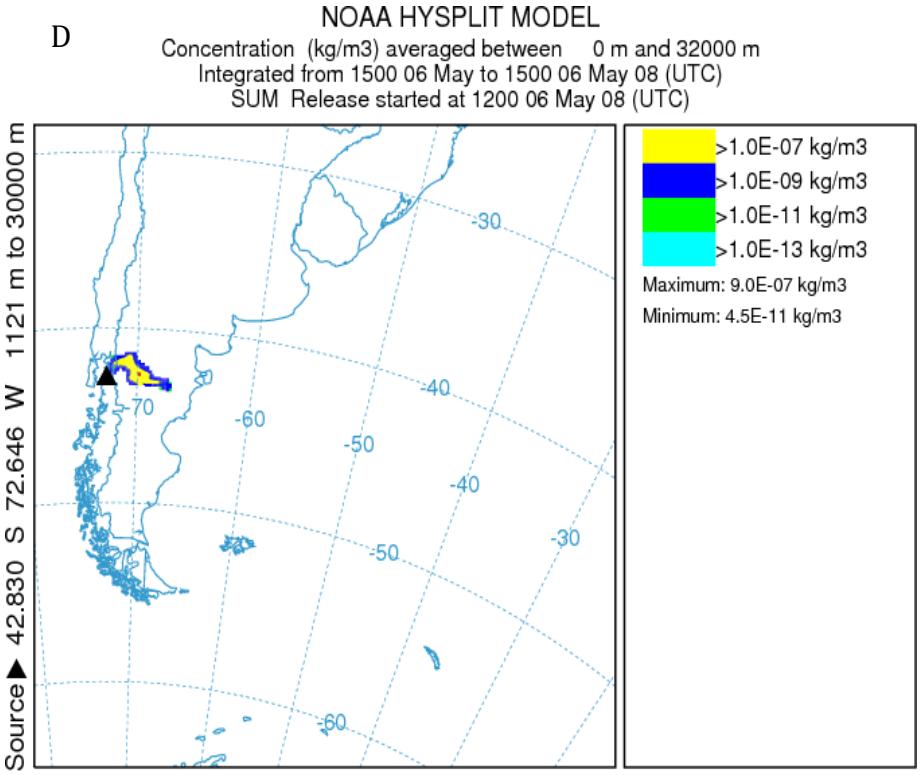
NOAA HYSPLIT MODEL
Concentration (kg/m3) averaged between 0 m and 32000 m
Integrated from 1500 06 May to 1500 06 May 08 (UTC)
SUM Release started at 1200 06 May 08 (UTC)
Source ▲ 42.830 S 72.646 W 1121 m to 30000 m
>1.0E-07 kg/m3
>1.0E-09 kg/m3
>1.0E-11 kg/m3
>1.0E-13 kg/m3
Maximum: 9.0E-07 kg/m3
Minimum: 4.5E-11 kg/m3

E

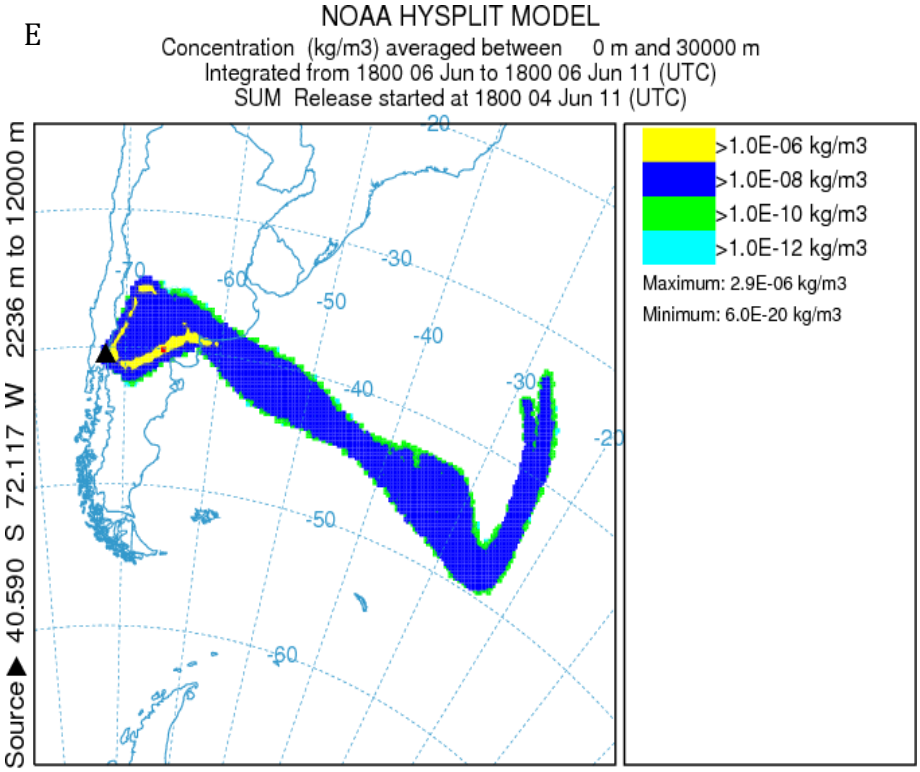
NOAA HYSPLIT MODEL
Concentration (kg/m3) averaged between 0 m and 30000 m
Integrated from 1800 06 Jun to 1800 06 Jun 11 (UTC)
SUM Release started at 1800 04 Jun 11 (UTC)
Source ▲ 40.590 S 72.117 W 2236 m to 12000 m
>1.0E-06 kg/m3
>1.0E-08 kg/m3
>1.0E-10 kg/m3
>1.0E-12 kg/m3
Maximum: 2.9E-06 kg/m3
Minimum: 6.0E-20 kg/m3

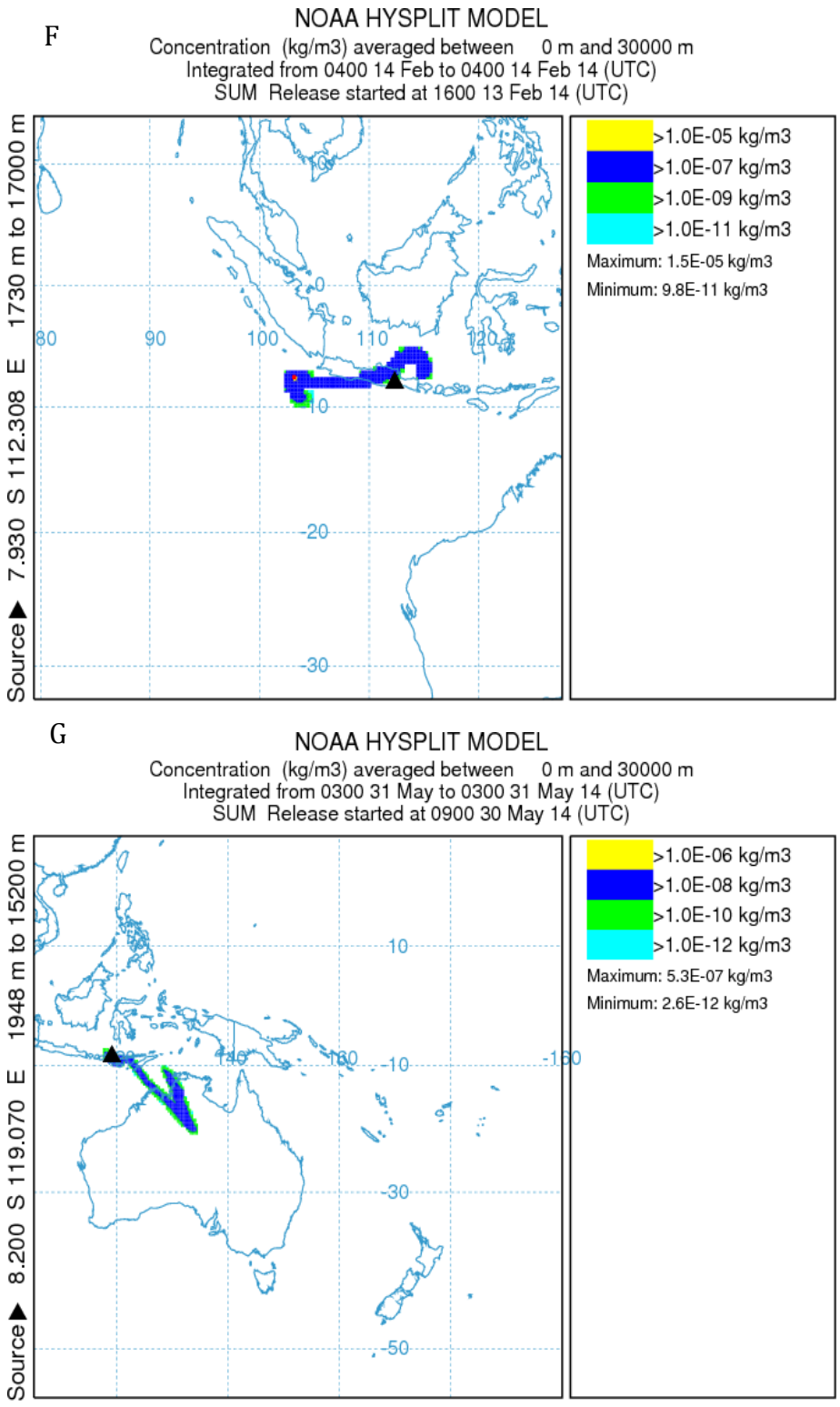

Figure 5: Ash concentrations (kg/m^3) were obtained via HYSPLIT for the following eruptions and times: (A) Kasatochi, August 9, 2008, 0100Z; (B) Okmok, July 12, 2008, 2300Z; (C) Grímsvötn, May 23, 2011, 1300Z; (D) Chaitén, May 6, 2008, 1500Z; (E) Puyehue-Cordón Caulle, June 6, 2011, 1800Z; (F) Kelut, February 14, 2014, 0400Z; (G) Sangeang Api, May 31, 2014, 0300Z

3.5 Description of back-propagation neural network

A neural network, or a structure that mathematically identifies relationships between given inputs and outputs (Hsu et al., 1995), is made up of neurons, which consist of input signals, a set of weights, activation levels, and threshold functions (Luger and Stubblefield, 1998). Neural networks have varying topologies, learning algorithms, and encoding schemes (Luger and Stubblefield, 1998). This particular study used a back-propagation learning algorithm for a multi-layer neural network, which propagates error backwards starting from the output layer through the hidden layers, which connect the input and output layers (Luger and Stubblefield, 1998).

In this multi-layer network, neurons, which are connected in layers, pass their activations only to the following layer. Since this can result in widespread error, a back-propagation learning algorithm is used to determine the weight distribution that results in the least amount of error (Luger and Stubblefield, 1998). The amount of error is easily determined for the output nodes, as it is just the difference between the desired and observed output values (Equation 1):

$$d_i - O_i \tag{1}$$

However, it is more difficult to determine the amount of error within hidden layers (Luger and Stubblefield, 1998). A logistic function, or activation function, is used because it has a sigmoid shape, is continuous, and because it can determine the nodes with the most error (Equation 2):

$$f(\text{net}) = \frac{1}{1 + e^{-\lambda * net}} \tag{2}$$

where

$$\text{net} = \Sigma w_i x_i \tag{3}$$

and x_i represents the input on line i, w_i represents the weight on line i, and λ is a parameter used to adjust the curve of the sigmoid (Luger and Stubblefield, 1998). Back-propagation uses a gradient descent approach to determine the direction on an error surface where the error is most rapidly reduced. The error surface represents cumulative error as a function the neural network weights (Luger and Stubblefield, 1998). To determine the weight adjustments for back-propagation training (the k^{th} weight of the i^{th} node), the following formulae are used (Equations 4-5):

$$\Delta w_{ik} = -c(d_i - O_i) * O_i(1 - O_i)x_{ik} \tag{4}$$

is used for output layer nodes, and

$$\Delta w_{ik} = -c * O_i(1 - O_i)\Sigma(-\text{delta}_j * w_{ij})x_{ij} \tag{5}$$

is used for hidden layer nodes, where j represents the nodes in the following layer affected by i's signals and where

$$\text{delta}_j = \frac{\delta \text{Error}}{\delta \text{net}_j} = (d_i - O_i) * O_i\,(1 - O_i) \tag{6}$$

The weight adjustments for output layer nodes (Equation 4) are determined by first considering the mean squared network error, then taking the partial derivative of total error with respect to each output unit, followed by considering the partial derivative of the error at each node with respect to the weight at that particular node, and finally by taking the partial derivative of the actual output with respect to each weight (Luger and Stubblefield, 1998). To compute the weight adjustments for the hidden layer nodes (Equation 5), only one hidden layer is initially assumed and a single node's contribution to the total network error is analyzed. The contributions are summed across all nodes on the output layer, and the contribution of the k^{th} input weight on node i to the network

error is determined by first taking the partial derivative of the total network error with respect to the node i's output on the hidden layer. This is used to analyze the sensitivity of the total network error on the output layer to the updated weights on hidden node i (Luger and Stubblefield, 1998). Both Equations 4 and 5 are negative because the weight changes must be in the direction of the negative gradient, according to the minimization of error (Luger and Stubblefield, 1998). This process is repeated throughout the hidden layers.

3.6 Neural network training

Two back-propagation neural networks were used to determine whether or not ash or SO_2-rich ash was present in a given MODIS pixel. From 120 MODIS granules, 14 cases were chosen where HYSPLIT output was well aligned with satellite observations (Appendix B). Three masks were applied to each granule to create a selection of pixels

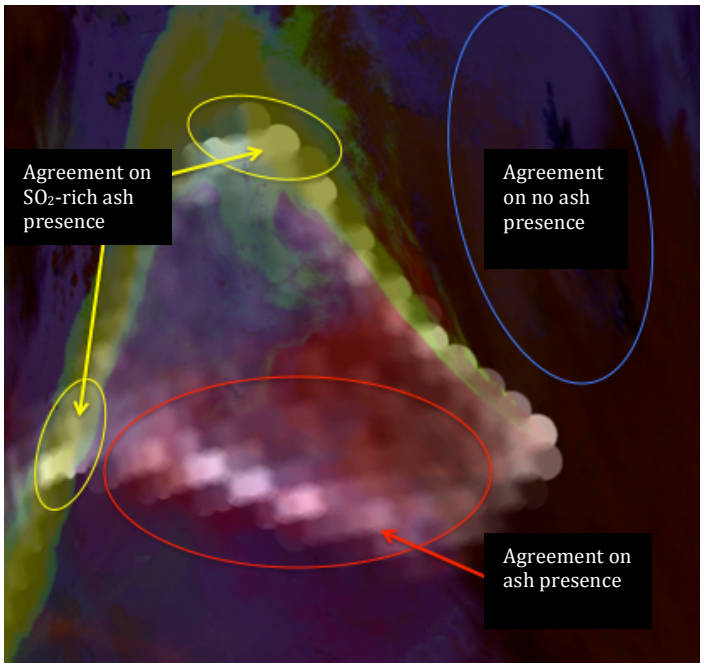

Figure 6: HYSPLIT output was overlaid onto MODIS granules for cases where MODIS and HYSPLIT were well aligned to select regions of interest. These regions of interest were used as masks to select only those areas of ash, no ash, SO_2-rich ash, and no SO_2-rich ash where HYSPLIT and MODIS were in agreement.

containing only ash, a selection containing only SO_2-rich ash, and a selection containing all other situations where ash was not present (Figure 6). The neural network created to differentiate between ash and no ash is referred to as the "red" neural network, and the network created to differentiate between SO_2-rich ash and no SO_2-rich ash is referred to as the "yellow" neural network. Both networks were trained using inputs obtained via the following band combinations: 12-11-μm brightness temperature difference, 11-8.6-μm brightness temperature difference, 11-7.3-μm brightness temperature difference, and 11-μm brightness temperature. Using the ash concentrations determined via HYSPLIT, two sets of flags were created to differentiate between ash (1) and no ash (0), and SO_2-rich ash (1) and no SO_2-rich ash (0). As validation, the neural networks used these flag as outputs. In Table 2, an excerpt from the training dataset used in the "red" neural network, the first column contains the 12-11-μm brightness temperature differences, the second column contains the 11-8.6-μm brightness temperature differences, the third column contains only the 11-μm brightness temperatures, the fourth contains the 11-7.4-μm brightness temperature difference, and the fifth column contains the previously mentioned flag to differentiate between ash and no ash.

12-11-µm (K)	11-8.6-µm (K)	11-µm (K)	11-7.3-µm (K)	Ash (1)/No Ash (0)
2.3	-0.49	266.18	10.17	1
-0.66	-3.66	227.18	-0.92	0
-2.07	2.52	294.54	40.65	0
-0.29	-1.63	268.84	16.79	1
-0.65	2.27	295.42	25.66	0
0.25	-1.7	245.36	0.08	1
-0.06	1.74	279.41	22.48	0
2.19	-0.09	273.01	16.06	1
-1.1	0.65	278.21	25.77	0
1.9	-0.74	273.77	16.32	1
-0.95	-0.67	256.09	7.33	0
3.71	-1.13	262.54	6.71	1
1.42	-0.92	272.21	16.39	1
-0.19	2.07	282.69	25.64	0
0.69	1.44	276.53	22.07	1
0.46	-4.07	215.62	-5.36	1
-1.3	-1.23	247.54	6.87	0
0.23	-0.84	242.49	-0.02	1
0.08	2.22	282.03	21.32	0

Table 2: An excerpt from the training dataset used in the "red" neural network. Columns 1-4 represent the neural network input and column 5 is representative of the output.

The back-propagation neural network settings used in this study are recorded in Appendix C. Most settings were kept at default, which include the number of repetitions, subset size of the train data, percentage of used test data, shift size of subset size, threshold options, the number of hidden neurons, the option to add noise to the data, and other options described below. The number of repetitions was set to 100, 10% of the training data was used, and 100% of the test data was used for both networks. The shift size, which allows the train subset to be shifted over the train dataset by a factor, was kept default, or to 5%. The threshold settings were kept at default: If the correlation coefficient associated with the training dataset was larger than the threshold, the window size was increased by 1%; If there was no modification, the window was set to shift after

each cycle. Correlation threshold was set to 96% and the "no modification" threshold was set to 0.0005%, which are both default settings. The number of hidden neurons was set to 25 for both the "red" and "yellow" networks. The gamma option, which defines the learning parameter, was set to 0, which makes the learning parameter equal to 10^0, or 1. Alpha was set to 4 to make the acceleration parameter equal to 0.4. The temperature, which controls the steepness of the sigmoid, was set to 10. No noise was added to the data. Dr. René Preusker, Institute for Space Sciences, Free University of Berlin, Germany, created the software used in this study for the training of this particular neural network.

CHAPTER 4

RESULTS

4.1 Optimal Thresholds

The neural network output was compared to the test dataset output for both the yellow and red networks. A Heidke skill score (HSS), a scoring method for measuring success where a perfect score is equal to one, was calculated for all possible ash/no ash and SO_2-rich ash/no SO_2-rich ash thresholds to determine optimal thresholds (Figure 7).

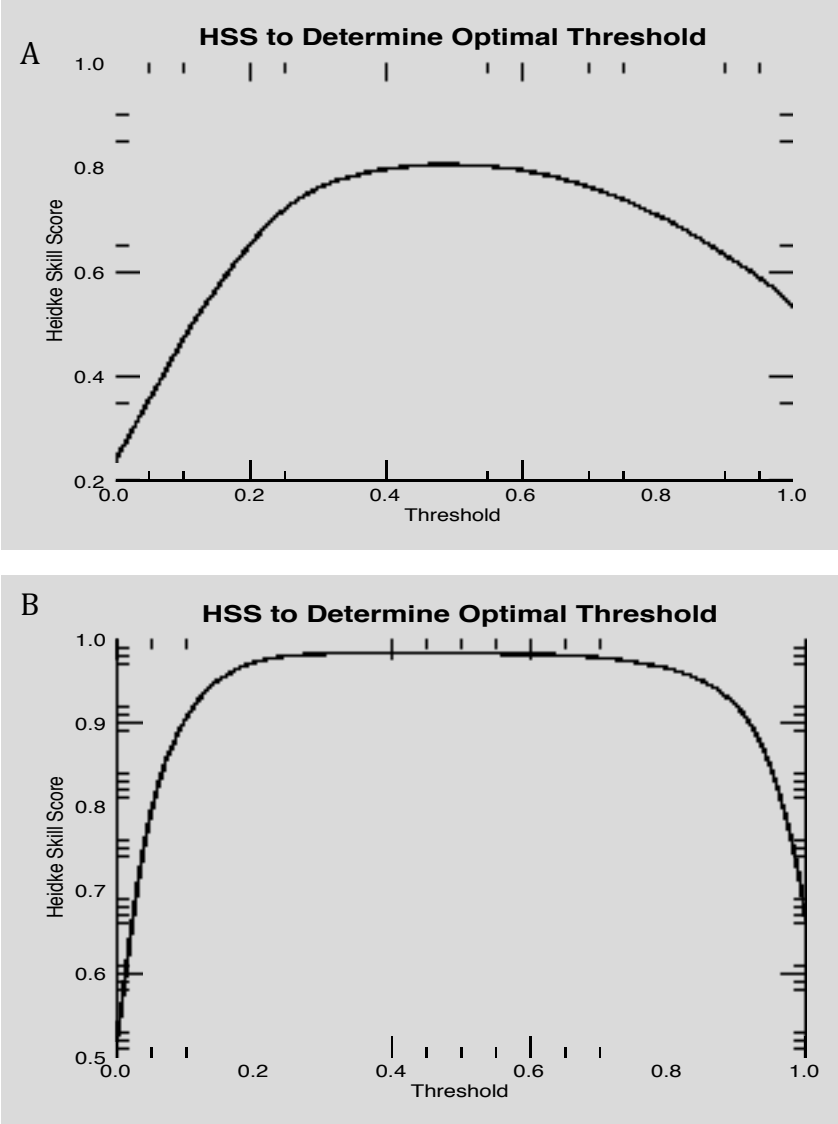

Figure 7: (A) Optimal threshold for ash retrieval determined to be 0.48 with Heidke skill score of 0.81; (B) Optimal threshold for SO_2-rich ash retrieval determined to be 0.47 with Heidke skill score of 0.98.

The optimal thresholds for ash retrieval and SO_2-rich ash retrieval were 0.48 and 0.47, respectively. The yellow neural network was found to a higher Heidke Skill score than the red neural network, and thus less error (Table 3-4).

Ash Observed	Ash Predicted		SO_2-rich Ash Observed	SO_2-Rich Ash Predicted	
	No	Yes		No	Yes
No	87.7%	12.3%	No	98.4%	1.6%
Yes	6.8%	93.2%	Yes	0.03%	99.97%

Table 3: (Red) Red neural network (ash-detection) output was compared the test dataset output to measure success.

Table 4: (Yellow) Yellow neural network (SO_2-rich ash detection) output was compared the test dataset output to measure success.

Of all data containing volcanic ash, 93% of pixels are correctly identified and 7% are incorrectly flagged (Table 3). Out of the all data containing SO_2-rich ash, almost 100% are correctly identified (Table 4).

4.2 Neural Network Output

Using the optimal thresholds determined by the Heidke skill score test, MODIS granules for the specified eruptions were fed to the neural network to create new images locating areas of ash, no ash, SO_2-rich ash, and no SO_2-rich ash (Figure 8).

A

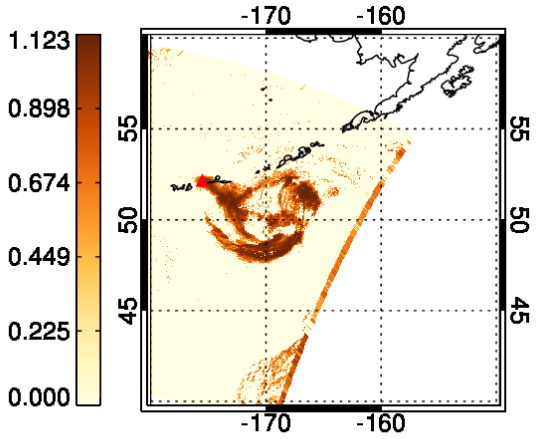
1.123
0.898
0.674
0.449
0.225
0.000
-170
-160
55
50
45

B

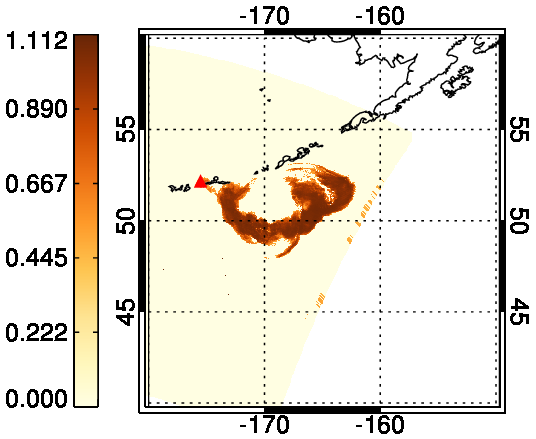
1.112
0.890
0.667
0.445
0.222
0.000
-170
-160
55
50
45

C

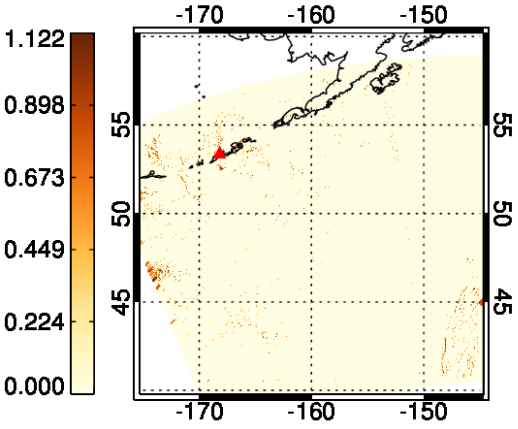
1.122
0.898
0.673
0.449
0.224
0.000
-170
-160
-150
55
50
45

D

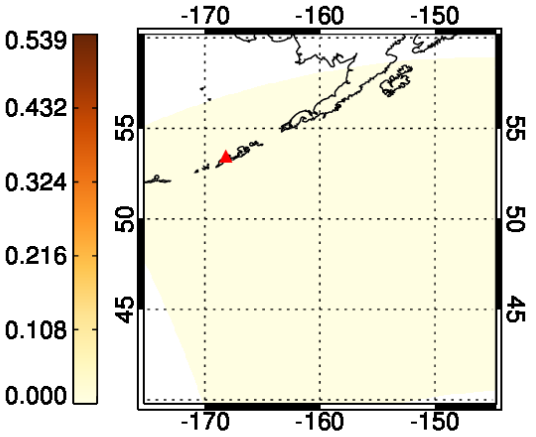
0.539
0.432
0.324
0.216
0.108
0.000
-170
-160
-150
55
50
45

E

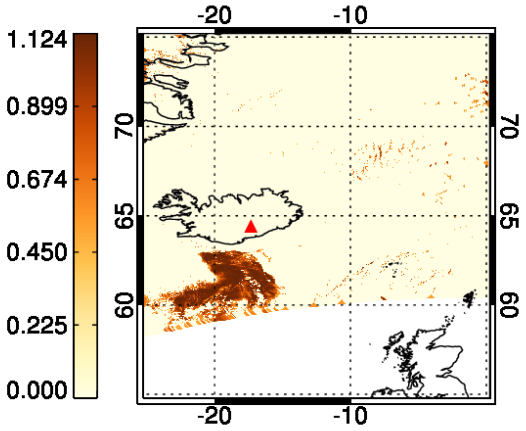
1.124
0.899
0.674
0.450
0.225
0.000
-20
-10
70
65
60

F

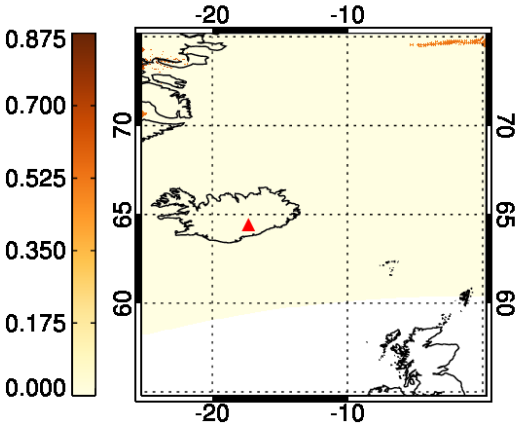
0.875
0.700
0.525
0.350
0.175
0.000
-20
-10
70
65
60

G

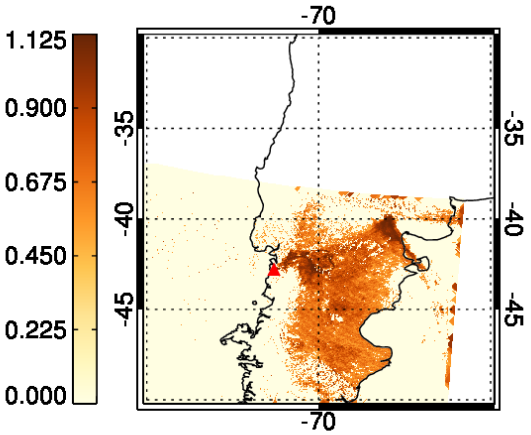
1.125
0.900
0.675
0.450
0.225
0.000
-70
-35
-40
-45

H

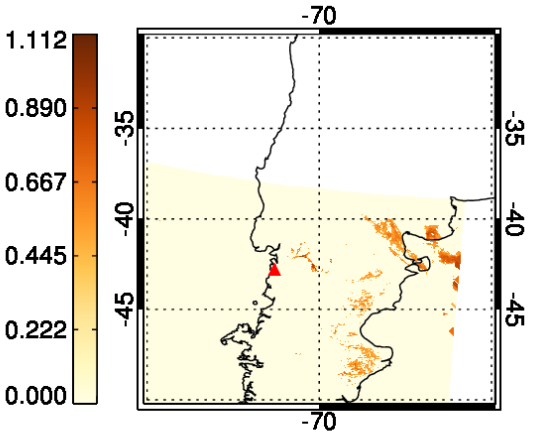
1.112
0.890
0.667
0.445
0.222
0.000
-70
-35
-40
-45

I

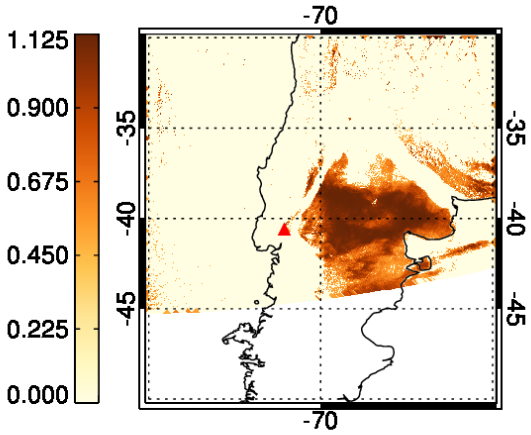
1.125
0.900
0.675
0.450
0.225
0.000
-70
-35
-40
-45

J

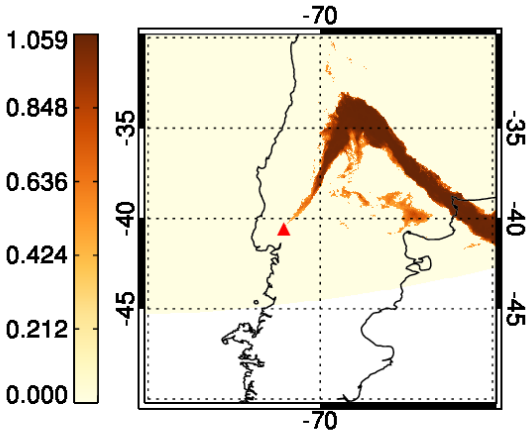
1.059
0.848
0.636
0.424
0.212
0.000
-70
-35
-40
-45

K

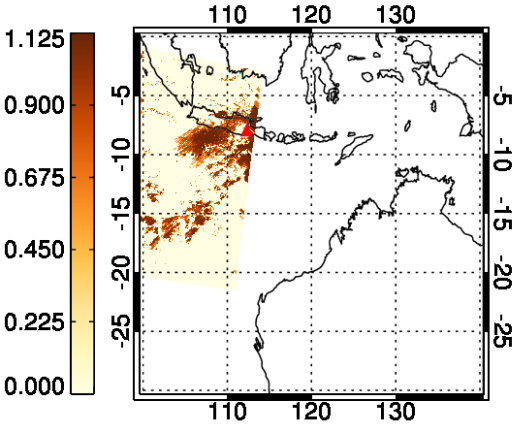
1.125
0.900
0.675
0.450
0.225
0.000
110
120
130
-5
-10
-15
-20
-25

L

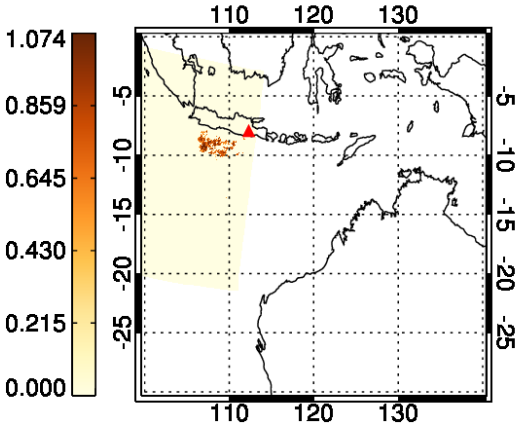
1.074
0.859
0.645
0.430
0.215
0.000
110
120
130
-5
-10
-15
-20
-25

M N

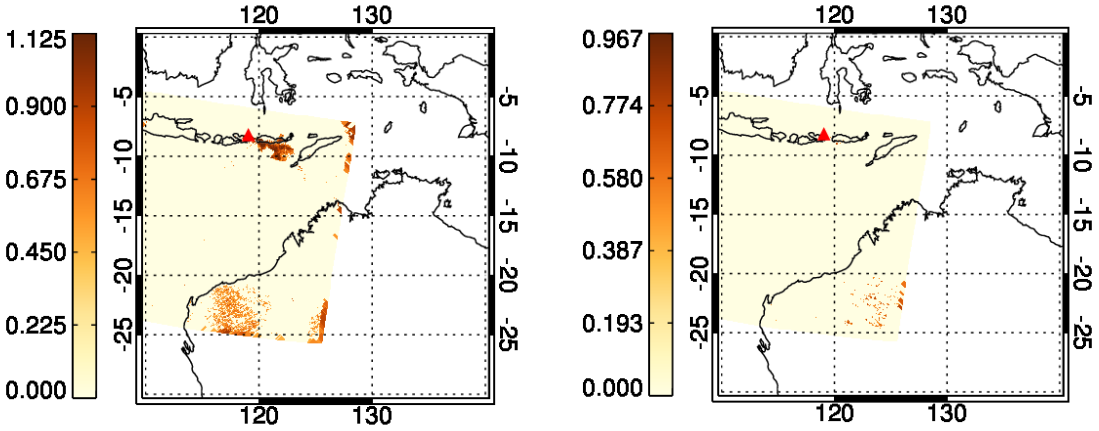

Figure 8: "Red" neural network output for the following eruptions and times: (A) Kasatochi, August 8, 2008, 2305Z; (C) Okmok, July 12, 2008, 2330Z; (E) Grímsvötn, May 23, 2011, 1400Z; (G) Chaitén, May 6, 2008, 1505Z; (I) Puyehue-Cordón Caulle, June 6, 2011, 1840Z; (K) Kelut, February 14, 2014, 0335Z; (M) Sangeang Api, May 31, 2014, 0235; "Yellow" neural network output images are located to the right of their corresponding "red" neural network output images: (B), (D), (F), (H), (J), (L), (N).

Referring back to the corresponding RGBs in Figure 4, the neural network output in Figure 8 differentiates the pink/red areas, representing ash in the RGBs, from the ambient environment and SO_2, and also differentiates the bright yellow, representing SO_2-rich ash in the RGBs, from the ambient environment and ash. Figures 8-A and 8-B correspond to Figures 4-A and 4-B, the eruption of Kasatochi in 2008. This particular volcanic cloud, 2 km thick, was located over a dense meteorological cloud system (Corradini et al., 2010). In the RGB, Figure 4-A, created using MODIS infrared bands, there is a significant SO_2-rich ash signal. Although this eruption was characterized by the highest SO_2 release since Hudson in 1991 (Lara, 2009), volcanic ash can reduce the radiance for all channels in the thermal infrared spectral range, leading to an overestimation of SO_2 (Corradini et al., 2009). In addition, when ash and SO_2 are

collocated or when SO_2 is located above ash, ash will appear bright yellow in RGBs created using the band combinations in Figure 3. This is due to the strong SO_2 absorption in 8.6 μm combined with the lack of absorption in 11 and 12 μm (Pavolonis, 2014).

Figures 8-C and 8-D correspond to Figures 4-C and 4-D, the eruption of Okmok, the second Aleutian Islands eruption analyzed in this particular study. This eruption is unique because it was phreatomagmatic, or characterized by high water content (GVP) This eruption incorporated ground water and water inside the caldera (GVP). The RGB in Figure 4-C is not characterized by the bright red/pink signature usually observed for ash, although a 15 km plume is reported (GVP) and an ash signature is clear in the visible image, Figure 4-D. When high amounts of water are incorporated into ash clouds, they lose their ash signature and begin to appear more like meteorological clouds than ash clouds (Prata, 2009), which explains why the neural network is not discerning the volcanic cloud in this particular case. There is also no SO_2-rich ash detected because a SO_2 signature is not present with this eruption at this time.

The eruption of Grímsvötn, 2011, depicted in Figures 8-E, 8-F, 4-E, and 4-F, occurred about 43 hours prior to the image in the figures. Two days earlier, ash at lower altitudes was observed to drift to the south while ash at higher altitudes drifted east (GVP). The next day, May 22, most ash drifted south and southwest (GVP). An ash signature is seen to the south of the volcano in both the RGB (Figure 4-E) and the visible image (Figure 4-F). An SO_2 signal is not observed in the RGB (Figure 4-E). The neural network detects ash in the correct location with little overestimation (Figure 8-E), and also does not place any SO_2 in the atmosphere at this particular time (Figure 8-F).

Chaitén, the first of two mid-latitude eruption analyzed in this study, is represented in Figures 8-G, 8-H, 4-G, and 4-H. Four days before this particular image was captured by MODIS, Chaitén erupted with a 21 km plume which drifted to the southeast, east, west, and northeast (GVP). A second eruption occurred on May 6, 2008, 12:32 UTC, about 2.5 hours prior to this image. At first glance, it would appear that the neural network is greatly overestimating ash east of the volcano. However, there are no high meteorological clouds in this region, as seen in Figure 4-H, and previous eruptions from days earlier contributed a significant portion of ash to the atmosphere. It is likely that the neural network is detecting low level ash from previous eruptions to the east of the volcano (Figure 8-G). A strong signal is also observed to the east-northeast of the volcano, likely from the previous plinian column erupting from this volcano on May 2, 2008 (Figure 8-G). The neural network detected little SO_2 (Figure 8-H), as this particular eruption was not characterized by high SO_2 emissions (Lara, 2009, Carn et al., 2009).

Figures 8-I, 8-J, 4-I, and 4-J depict the volcanic cloud resulting from Puyehue-Cordón Caulle about 48 hours after the initial eruption. On June 4, 2011, ash located at 5 km drifted to the south while ash at 10 km drifted west and east (GVP). On this same day gas was observed drifting west while ash drifted east-southeast (GVP). Ash was again observed drifting east-southeast on June 5, 2011. Winds shifted on June 6, 2011, and ash drifted to the east-northeast while a previous volcanic cloud continued east-southeast over the ocean (GVP). The neural network detects both faint and strong ash signatures in Figure 8-I, while not overestimated in the presence of high meteorological clouds to the west of the volcano. The neural network distinguishes the SO_2-rich cloud from the ambient atmosphere with clear boundaries and little overestimation (Figure 8-J).

Neural network output for the eruption of Kelut is shown in Figures 8-K and 8-L, which correspond to the RGB and visible image in Figures 4-K and 4-L, respectively. This particular image was captured by MODIS about 3 hours after the initial eruption. The 17 km plume was observed drifting northeast, northwest, and west. Upon analysis of the RGB (Figure 4-K), it is difficult to differentiate the ash cloud from surrounding meteorological clouds. As this volcano is located in the tropics, characterized by high atmospheric water vapor, this is not surprising. *Kristiansen et al.* [2015] found this volcanic cloud difficult to detect within the first several hours of eruption due to the thickness of the ash cloud combined with the high amounts of ice coating within meteorological clouds. However, the SO_2 signal is easily distinguishable from the ambient environment in both the RGB (Figure 4-K) and the neural network output (Figure 8-L).

Figures 8-M, 8-N, 4-M, and 4-N depict the volcanic cloud that erupted from Sangeang Api about 18 hours after the initial eruption. The initial plume was observed drifting west at 3 km altitude and east-southeast at 15.2 km altitude (GVP). A bright pink ash signal is observed to the east-southeast in the RGB, and the same signal is observed as brown in the visible image (Figure 4-M, 4-N), collaborating weekly reports (GVP). However, a pink signal is also observed over West Australia. This is most likely dust from the deserts of Australia, as dust has similar radiative properties to volcanic ash. No SO_2 signal is observed in the RGB (Figure 4-M). The neural network distinguishes ash from the ambient environment, but overestimates in the presence of dust (Figure 8-M). The neural network correctly places no SO_2 signal in this particular observation (8-N).

CHAPTER 5

DISCUSSION

In this study a neural network-based algorithm was developed to detect volcanic ash and SO_2-rich ash using MODIS observations. However, the neural network shows significantly less accuracy when the volcanic cloud is characterized by high water or ice content or when surrounded by water or ice-rich meteorological clouds. As water, ice, and water vapor can act to mask the ash signal, the accuracy of ash retrievals is highly dependent on the amount for water vapor in the atmosphere (Watson et al., 2004). Because of this, the neural network is likely to have a higher accuracy in dry atmospheres. High, ice-rich meteorological clouds that are observed to lead to significant ash overestimation are present in Figures 4-A and 4-K. In addition to water vapor adjusting the amounts of ash detected, SO_2 can also mask a volcanic ash signal, as mentioned in the previous section (Pavolonis, 2014). In the event that SO_2 and ash are collocated, or when SO_2 is located above ash, it is helpful to use visible images (MODIS bands 1, 4, 3) to determine if an ash signal is present in the visible image in the same location as the SO_2 signal in the RGB. This method, however, cannot be used at night. Ash is also overestimated in the presence of high dust concentrations, as seen in Figure 4-M, as dust over West Australia is incorrectly classified as ash. Overestimations that have not yet been mentioned are located on the edges of the MODIS swath, which occur likely due to unfavorable satellite observation angles. This overestimation has not been corrected in this particular network, but will be addressed in the next trained network.

In order to train the network, HYSPLIT was treated to be representative of reality. This may not always be accurate, especially for eruptions characterized by multiple eruptive pulses. One of the limitations of HYSPLIT is that it can only be used with one eruptive pulse or one continuous ash release. Chaitén, which was characterized by two significant eruptive pulses four days apart, was one case where HYSPLIT and MODIS were not well aligned. The second pulse was analyzed in this study, but low level ash was still present in the atmosphere from the previous eruption. HYSPLIT had no way of knowing this, which could lead to missed ash within the training of the neural network. Another limitation of this study is the lack of knowledge about erupted ash quantity from some events. When unknown, USGS parameters were used, which could lead to significant errors within HYSPLIT and thus the training of the neural network.

The location of volcanic ash in the atmosphere is crucial information for the aviation industry, as volcanic ash can heavily damage jet engines and other parts of aircraft, as discussed in Section 2.6. This particular study can be used to automatically detect ash in MODIS observations, providing critical information to the aviation industry. However, this study does not yet provide information about the concentration of ash in each pixel or the altitude of the ash. Currently, this study only provides confirmation of the presence of ash and/or SO_2-rich ash within a 30 km vertical column.

Future work will include determining the accuracy of training an additional neural network to detect not only whether or not ash is present, but also ash concentration and ash cloud altitude.

APPENDIX

A. HYSPLIT Parameters

Kasatochi

- Meteorological Data: Reanalysis (global, 1948-present)
- Volcano: Kasatochi: Aleutian Islands
- Use USGS-assigned Eruption Source Parameters (ESP)? No
- GDAS1 Meteorological File: RP200808.gbl
- Input units: meters
- Number of concentration layers: 1
- Deposition/Ashfall: Yes
- Option to change particle size distribution: No
- Use non-uniform vertical ash distribution: No
- Calculate eruption rate from eruption height: No
- Other HYSPLIT options: No
- Start time (UTC): 08/08/2008, hour 4
- Source Latitude: 52.177
- Source Longitude: -175.5
- Ash column top: 19 km (Pavolonis, personal communication)
- Ash column bottom: 313 m (summit)
- Eruption duration:1 hour
- Eruption ash quantity: 1 Tg (1,000,000,000 kg) (Pavolonis, personal communication)
- Total duration: 48 hours
- Sampling type: Snapshot
- Average period/Snapshot interval: 3
- Concentration Grid Resolution (decimal degrees): -1
- Concentration grid domain size (decimal degrees): -1, -1
- Top of layer: 30000 m
- Bottom of layer: 0 m
- Wet del of particle: 3.2E+05, 5.0E-05
- Sum deposition over total run time? Yes
- Ash bulk density? 2.5 grams/cubic cm
- Deposition/Ashfall Output units: mass/area
- Concentration output units: kg/cubic m
- Plot projection: default
- Plot resolution: 96
- Zoom factor: 70
- US county borders?: No
- Google Earth output of contours?: No
- PS file?: Yes
- Create PDF file of graphics?: Yes

Okmok

- Meteorological Data: Reanalysis (global, 1948-present)
- Volcano: Okmok: Aleutian Islands
- Use USGS-assigned Eruption Source Parameters (ESP)? No
- GDAS1 Meteorological File: RP200807.gbl
- Input units: meters
- Number of concentration layers: 1
- Deposition/Ashfall: Yes
- Option to change particle size distribution: No
- Use non-uniform vertical ash distribution: No
- Calculate eruption rate from eruption height: No
- Other HYSPLIT options: No
- Start time (UTC): 07/12/2008, hour 20
- Source Latitude: 53.43
- Source Longitude: -168.13
- Ash column top: 15000 m (GVP)
- Ash column bottom: 1072 m (summit)
- Eruption duration: 1 hour
- Eruption ash quantity: 0.07 Tg (Prata et al., 2010)
- Total duration: 48 hours
- Sampling type: Snapshot
- Average period/Snapshot interval: 3
- Concentration Grid Resolution (decimal degrees): -1
- Concentration grid domain size (decimal degrees): -1, -1
- Top of layer: 30000
- Bottom of layer: 0
- Wet del of particle: 3.2E+05, 5.0E-05
- Sum deposition over total run time? Yes
- Ash bulk density? 2.5 grams/cubic cm
- Deposition/Ashfall Output units: mass/area
- Concentration output units: kg/cubic m
- Plot projection: Default
- Plot resolution: 96
- Zoom factor: 70
- US county borders?: No
- Google Earth output of contours?: No
- PS file?: Yes
- Create PDF file of graphics?: Yes

Grímsvötn

- Meteorological Data: Reanalysis (global, 1948-present)
- Volcano: Grimsvotn: Iceland-NE
- Use USGS-assigned Eruption Source Parameters (ESP)? No
- GDAS1 Meteorological File: RP201105.gbl

- Input units: meters
- Number of concentration layers: 1
- Desposition/Ashfall: Yes
- Option to change particle size distribution: No
- Use non-uniform vertical ash distribution: No
- Calculate eruption rate from eruption height: No
- Other HYSPLIT options: No
- Start time (UTC): 05/21/2011, Hour 19
- Source Lat: 64.43
- Source Long: -17.33
- Ash column top: 20000 m
- Ash column bottom: 1724 m (summit)
- Eruption duration: 24 hours (Moxnes et al., 2014)
- Eruption ash quantity: 0.4 Tg (400,000,000 kg) (Moxnes et al., 2014)
- Total duration: 48 hours
- Sampling type: Snapshot
- Average period/Snapshot interval: 3 hours
- Concentration Grid Resolution (decimal degrees): -1
- Concentration grid domain size (decimal degrees): -1, -1
- Top of layer: 30000 m
- Bottom of layer: 0
- Wet del of particle: 3.2E+05, 5.0E-05
- Sum deposition over total run time? Yes
- Ash bulk density? 2.5 grams/cubic cm
- Deposition/Ashfall Output units: /area
- Concentration output units : kg/cubic m
- Plot projection: Default
- Plot resolution: 96
- Zoom factor: 70
- US county borders?: No
- Google Earth output of contours?: No
- PS file?: Yes
- Create PDF file of graphics?: Yes

Chaitén

- Meteorological Data: Reanalysis (global, 1948-present)
- Volcano: Chaiten: Chile-S
- Use USGS-assigned Eruption Source Parameters (ESP)? No
- GDAS1 Meteorological File: RP200805.gbl
- Input units: meters
- Number of concentration layers: 1
- Deposition/Ashfall: Yes
- Option to change particle size distribution: No
- Use non-uniform vertical ash distribution: No
- Calculate eruption rate from eruption height: No

- Other HYSPLIT options: No
- Start time (UTC): 05/06/2008, Hour 12
- Source Latitude: -42.83
- Source Longitude: -72.646
- Ash column top: 30000 m (GVP)
- Ash column bottom: 1121 m (summit height)
- Eruption duration: 1 hour
- Eruption ash quantity: 0.2 Tg (200,000,000 kg) (Durant et al., 2012)
- Total duration: 24 hours
- Sampling type: Snapshot
- Average period/Snapshot interval: 3 hours
- Concentration Grid Resolution (decimal degrees): -1
- Concentration grid domain size (decimal degrees): -1, -1
- Top of layer: 32000 m
- Bottom of layer: 0
- Wet del of particle: 3.2E+05, 5.0E-05
- Sum deposition over total run time? Yes
- Ash bulk density? 2.5 grams/cubic cm
- Deposition/Ashfall Output units: mass/area
- Concentration output units: kg/cubic meter
- Plot projection: Default
- Plot resolution: 96 dpi
- Zoom factor: 70
- US county borders?: No
- Google Earth output of contours?: no
- PS file?: yes
- Create PDF file of graphics?: yes

Puyehue-Cordón Caulle

- Meteorological Data: Reanalysis (global, 1948-present)
- Volcano: Puyehue Cordon Caulle: Chile-C
- Use USGS-assigned Eruption Source Parameters (ESP)? No
- GDAS1 Meteorological File: RP201106.gbl
- Input units: meters
- Number of concentration layers: 1
- Deposition/Ashfall: Yes
- Option to change particle size distribution: No
- Use non-uniform vertical ash distribution: No
- Calculate eruption rate from eruption height: No
- Other HYSPLIT options: No
- Start time (UTC): 06/04/2011, Hour 18
- Source Latitude: -40.56
- Source Longitude: -72.117
- Ash column top: 12000 m (GVP)
- Ash column bottom: 2236 m (summit)

- Eruption duration: 48 hours
- Eruption ash quantity: 17280000000 kg (USGS ESP)
- Total duration: 48 hours
- Sampling type: Snapshot
- Average period/Snapshot interval: 3 hours
- Concentration Grid Resolution (decimal degrees): -1
- Concentration grid domain size (decimal degrees): -1, -1
- Top of layer: 30000 m
- Bottom of layer: 0 m
- Wet del of particle: 3.2E+05, 5.0E-05
- Sum deposition over total run time? Yes
- Ash bulk density? 2.5 grams/cubic cm
- Deposition/Ashfall Output units: mass/area
- Concentration output units: kg/cubic m
- Plot projection: Default
- Plot resolution: 96
- Zoom factor: 70
- US county borders?: No
- Google Earth output of contours?: No
- PS file?: Yes
- Create PDF file of graphics?: Yes

Kelut

- Meteorological Data: Reanalysis (global, 1948-present)
- Volcano: Kelut: Java
- Use USGS-assigned Eruption Source Parameters (ESP)? No
- GDAS1 Meteorological File: RP201402.gbl
- Input units: meters
- Number of concentration layers: 1
- Deposition/Ashfall: Yes
- Option to change particle size distribution: No
- Use non-uniform vertical ash distribution: No
- Calculate eruption rate from eruption height: No
- Other HYSPLIT options: No
- Start time (UTC): 02/13/2014, Hour 16
- Source Latitude: -7.93
- Source Longitude: 112.308
- Ash column top: 17000 m (GVP)
- Ash column bottom: 1730 m (summit)
- Eruption duration: 1 hour
- Eruption ash quantity: 17280000000 kg (USGS ESP)
- Total duration: 48 hours
- Sampling type: Snapshot
- Average period/Snapshot interval: 3 hours
- Concentration Grid Resolution (decimal degrees): -1

- Concentration grid domain size (decimal degrees): -1, -1
- Top of layer: 30000 m
- Bottom of layer: 0
- Wet del of particle: 3.2E+05, 5.0E-05
- Sum deposition over total run time? Yes
- Ash bulk density? 2.5 grams/cubic cm
- Deposition/Ashfall Output units: /area
- Concentration output units : kg/cubic m
- Plot projection: Default
- Plot resolution: 96
- Zoom factor:70
- US county borders?: No
- Google Earth output of contours?: No
- PS file?: yes
- Create PDF file of graphics?: yes

Sangeang Api

- Meteorological Data: Reanalysis (global, 1948-present)
- Volcano: Sangeang Api: Lesser Sunda Islands
- Use USGS-assigned Eruption Source Parameters (ESP)? No
- GDAS1 Meteorological File: RP201405.gbl
- Input units: meters
- Number of concentration layers: 1
- Desposition/Ashfall: Yes
- Option to change particle size distribution: No
- Use non-uniform vertical ash distribution: No
- Calculate eruption rate from eruption height: No
- Other HYSPLIT options: No
- Start time (UTC): 05/30/2014, Hour 9
- Source Lat: -8.2
- Source Long: 119.07
- Ash column top: 15200 m (GVP)
- Ash column bottom: 1948 m (summit)
- Eruption duration: 1 hour
- Eruption ash quantity: 864000000 kg (USGS ESP)
- Total duration: 48 hours
- Sampling type: Snapshot
- Average period/Snapshot interval: 3 hours
- Concentration Grid Resolution (decimal degrees): -1
- Concentration grid domain size (decimal degrees): -1, -1
- Top of layer: 30000 m
- Bottom of layer: 0
- Wet del of particle: 3.2E+05, 5.0E-05
- Sum deposition over total run time? Yes
- Ash bulk density? 2.5 grams/cubic cm
- Deposition/Ashfall Output units: /area

- Concentration output units : kg/cubic m
- Plot projection: Default
- Plot resolution: 96
- Zoom factor:70
- US county borders?: No
- Google Earth output of contours?: NO
- PS file?: yes
- Create PDF file of graphics?: yes

B. Neural Network Training Dataset

VOLCANO	OVERPASS (UTC) yyyy-mm-ddThh:mm:ss	SATELLITE	HYSPLIT TIME
Kasatochi	2008-08-08T13:40:00	Aqua	2008-08-08T13:00:00
Kasatochi	2008-08-08T23:05:00	Terra	2008-08-08T22:00:00
Kasatochi	2008-08-09T12:45:00	Aqua	2008-08-09T13:00:00
Kasatochi	2008-08-09T22:10:00	Terra	2008-08-09T22:00:00
Kasatochi	2008-08-09T23:55:00	Aqua	2008-08-09T22:00:00
Puyehue-Cordón Caulle	2011-06-05T05:55:00	Aqua	2011-06-05T06:00:00
Puyehue-Cordón Caulle	2011-06-05T17:55:00	Aqua	2011-06-05T18:00:00
Puyehue-Cordón Caulle	2011-06-06T03:20:00	Terra	2011-06-06T03:00:00
Puyehue-Cordón Caulle	2011-06-06T05:00:00	Aqua	2011-06-06T06:00:00
Puyehue-Cordón Caulle	2011-06-06T14:25:00	Terra	2011-06-06T15:00:00
Puyehue-Cordón Caulle	2011-06-06T18:40:00	Aqua	2011-06-06T18:00:00
Sangeang Api	2014-05-30T14:05:00	Terra	2014-05-30T15:00:00
Sangeang Api	2014-05-30T17:10:00	Aqua	2014-05-30T18:00:00
Sangeang Api	2014-05-31T02:35:00	Terra	2014-05-31T03:00:00

C. Neural Network Settings

"Red" Neural Network Settings:

- Number of repetitions: 100
- Size of used subset in % of train data: 10
- Percentage of used test data: 100
- Shift step in % of subset size: 5
- If_Threshold_Increase_Subset selected
- If_No_Modification_Shift_Subset selected
- Corr_threshold, transformed_data selected
- Threshold of correlation: 96
- Threshold of no_modification (%): 0.0005
- Number of hidden neurons: 25
- Gamma: 0
- Alpha: 4
- Temperature: 10
- I.-BIAS selected
- H.-BIAS selected
- No_Weight_Decay selected
- QCK selected

"Yellow" Neural Network Settings:

- Number of repetitions: 100
- Size of used subset in % of train data: 10
- Percentage of used test data: 100
- Shift step in % of subset size: 5
- If_Threshold_Increase_Subset selected
- If_No_Modification_Shift_Subset selected
- Corr_threshold, transformed_data selected
- Threshold of correlation: 96
- Threshold of no_modification (%): 0.0005
- Number of hidden neurons: 25
- Gamma: 0
- Alpha: 4
- Temperature: 10
- I.-BIAS selected
- H.-BIAS selected
- No_Weight_Decay selected
- QCK selected

REFERENCES

Achterberg, E. P., Moore, C. M., Henson, S. A., Steigenberger, S., Stohl, A., Eckhardt, S., Ryan-Keogh, T. J. (2013). Natural iron fertilization by the Eyjafjallajökull volcanic eruption. *Geophysical Research Letters*, *40* (5), 921-926.

Ackerman, S. A. (1997). Remote sensing aerosols using satellite infrared observations. *Journal of Geophysical Research, 102* (D14), 17069.

Ackerman, S. A., Schreiner, A. J., Schmit, T. J., Woolf, H. M., Li, J., & Pavolonis, M. (2008). Using the GOES Sounder to monitor upper level SO_2 from volcanic eruptions. *Journal of Geophysical Research, 113* (D14).

Albrecht, B. A. (1989). Aerosols, cloud microphysics, and fractional cloudiness. *Science*, *245* (4923), 1227-30.

Bennartz, R., personal communication, March 8, 2015.

Corradini, S., Merucci, L., Prata, . J., & Piscini, A. (2010). Volcanic ash and SO_2 in the 2008 Kasatochi eruption: Retrievals comparison from different IR satellite sensors. *Journal of Geophysical Research*, *115*.

Carn, S. A., Krueger, A. J., Krotkov, N. A., Yang, K., & Evans, K. (2009). Tracking volcanic sulfur dioxide clouds for aviation hazard mitigation. *Natural Hazards*, *51* (2), 325-343.

Carn, S. A., Pallister, J. S., Lara, L., Ewert, J. W., Watt, S., Prata, A. J., Villarosa, G. (2009). The Unexpected Awakening of Chaitén Volcano, Chile. *Eos, Transactions American Geophysical Union, 90*(24), 205-206.

Carn, S. A., & Prata, F. J. (2010). Satellite-based constraints on explosive SO_2 release from Soufrière Hills Volcano, Montserrat. *Geophysical Research Letters, 37* (19).

Carn, S. A., Schneider, D. J., Bluth, G. J., Kobs, S. E., Rose, W. I., & Ernst, G. G. (2002). On the separation of ash and sulfur dioxide in volcanic clouds. In *AGU Spring Meeting Abstracts* (Vol. 1, p. 03).

Diaz, S. B., Paladini, A. A., Braile, H. G., Dieguez, M. C., Deferrari, G. A., Vernet, M., & Vrsalovic, J. (2014). Global and direct UV irradiance variation in the Nahuel Huapi National Park (Patagonia, Argentina) after the eruption of Puyehue-Cordon Caulle (Chile). *Journal of Atmospheric and Solar-Terrestrial Physics*, *112* (0), 47-56.

Draxler, R. R. and Rolph, G. D.: HYSPLIT (Hybrid Single-Particle Lagrangian Integrated Trajectory) Model access via NOAA ARL READY Website (http://www.arl.noaa.gov/ready/hysplit4.html), NOAA Air Resources Laboratory, Silver Spring, MD, USA, 2003.

Durant, A. J., Villarosa, G., Rose, W. I., Delmelle, P., Prata, A. J., & Viramonte, J. G. (2012). Long-range volcanic ash transport and fallout during the 2008 eruption of Chaitén volcano, Chile. *Physics and Chemistry of the Earth, Parts A/B/C*, *45–46* (0), 50-64.

Fee, D., Steffke, A., & Garces, M. (2010). Characterization of the 2008 Kasatochi and Okmok eruptions using remote infrasound arrays. *Journal of Geophysical Research*, *115.*

Feltz, W. F., Bedka, K., Wimmers, A. J., Pavolonis, M., Bedka, S. M., & Ackerman, S. (2006). *Satellite-Derived Products to Enhance Aviation Nowcasting of Convection, Turbulence, and Volcanic Ash.* Paper presented at the 14th Conference on Satellite Meteorology and Oceanography.

Flanner, G., Gardner, S., Eckhardt, S., Stohl, A., & Perket, J. (2014). Aerosol radiative forcing from the 2010 Eyjafjallajökull volcanic eruptions. *Journal of Geophysical Research: Atmospheres*, *119*(15), 9481-9491.

Francis, P., Oppenheimer, C. *Volcanoes.* Oxford: Oxford UP, 2004. Print.

Global Volcanism Program (*GVP*). Smithsonian Institution. Web. 15 Apr. 2014.

Graf, H. F. (1992). Arctic radiation deficit and climate variability. *Climate Dynamics*, 7, 19–28.

Hsu, K., H. V. Gupta, and S. Sorooshian (1995), Artificial Neural Network Modeling of the Rainfall-Runoff Process, *Water Resour. Res.*, 31(10), 2517–2530.

ICAO (International Civil Aviation Organization) (2007), Manual on volcanic ash, radioactive material, and toxic chemical clouds (2nd edition). Doc 9691-AN/954.

Kalnay et al. (1996). The NCEP/NCAR 40-year reanalysis project, *Bull. Amer. Meteor*. Soc., 77, 437-470.

Klüser, L., Erbertseder, T., & Meyer-Arnek, J. (2012). Observation of volcanic ash from Puyehue Cordón Caulle with IASI. *Atmospheric Measurement Techniques*, *6*, 35-46.

Kravitz, B., & Robock, A. (2011). Climate effects of high-latitude volcanic eruptions: Role of the time of year. *Journal of Geophysical Research, 116* (D1).

Kristiansen, I., Prata, J., Stohl, A., & Carn, A. (2015). Stratospheric volcanic ash emissions from the 13 February 2014 Kelut eruption. *Geophysical Research Letters.*

Langmann, B. (2013). Volcanic ash versus mineral dust: Atmospheric processing and environmental and climate impacts. *ISRN Atmospheric Sciences*, *2013*, 1-17.

Langmann, B. (2014). On the role of climate forcing by volcanic sulphate and volcanic ash. *Advances in Meteorology*, *2014*, 1-17.

Lara, L. E. (2009). The 2008 eruption of the Chaitén volcano, Chile: A preliminary report. *Andean Geology*, *36*(1), 125-129.

Luger, G., & Stubblefield, W. (1998). *Artificial Intelligence: Structures and Strategies for Complex Problem Solving* (3rd ed.). Reading, MA: Addison Wesley Longman.

Mastin, L.G., Guffanti, M., Ewert, J.E., and Spiegel, J., 2009, Preliminary spreadsheet of eruption source parameters for volcanoes of the world: U.S. Geological Survey Open-File Report 2009-1133, v. 1.2, 25 p.

Moxnes, E. D., Kristiansen, N. I., Stohl, A., Clarisse, L., Durant, A., Weber, K., & Vogel, A. (2014). Separation of ash and sulfur dioxide during the 2011 Grímsvötn eruption. *Journal of Geophysical Research: Atmospheres.*

Newhall, C. G., & Self, S. (1982). The Volcanic Explosivity Index (VEI) an estimate of explosive magnitude for historical volcanism. *Journal of Geophysical Research, 87* (C2), 1231.

Oman, L., Robock, A., Stenchikov, G., Schmidt, G. A., & Ruedy, R. (2005). Climatic response to high-latitude volcanic eruptions. *Journal of Geophysical Research-Atmospheres, 110*(D13).

Oman, L., Robock, A., Stenchikov, G. L., & Thordarson, T. (2006). High-latitude eruptions cast shadow over the African monsoon and the flow of the Nile. *Geophysical Research Letters, 33*(18).

Pavolonis, M.J., personal communication, September 12, 2014.

Pavolonis, M. J., Heidinger, A. K., & Sieglaff, J. (2013). Automated retrievals of volcanic ash and dust cloud properties from upwelling infrared measurements. *Journal of Geophysical Research: Atmospheres*, *118* (3), 1436-1458.

Pavolonis, M. (2014). Development of Satellite Remote Sensing Techniques for Quantifying Volcanic Ash Cloud Properties (Ph.D. Dissertation). University of Wisconsin-Madison.

Pavolonis, M. J., Feltz, W. F., Heidinger, A. K., & Gallina, G. M. (2006). A daytime complement to the reverse absorption technique for improved automated detection of volcanic ash. *Journal of Atmospheric & Oceanic Technology*, *23*(11).

Petersen, G. N., Bjornsson, H., Arason, P., & Löwis, S. V. (2012). Two weather radar time series of the altitude of the volcanic plume during the may 2011 eruption of Grímsvötn, Iceland. *Earth System Science Data Discussions*, *5*(1), 281-299.

Prata, A. J. (2009). Satellite detection of hazardous volcanic clouds and the risk to global air traffic. *Natural Hazards*, *51* (2), 303-324.

Prata, A. J., & Bernardo, C. (2007). Retrieval of volcanic SO_2 column abundance from Atmospheric Infrared Sounder data. *Journal of Geophysical Research, 112*(D20).

Prata, A. J., Carn, S. A., Stohl, A., & Kerkmann, J. (2007). Long range transport and fate of a stratospheric volcanic cloud from Soufrière Hills volcano, Montserrat. *Atmos. Chem. Phys., 7*(19), 5093-5103.

Prata, A. J., Gangale, G., Clarisse, L., & Karagulian, F. (2010). Ash and sulfur dioxide in the 2008 eruptions of Okmok and Kasatochi: Insights from high spectral resolution satellite measurements. *Journal of Geophysical Research, 115*.

Prata, A. J., & Kerkmann, J. (2007). Simultaneous retrieval of volcanic ash and SO_2 using MSG-SEVIRI measurements. *Geophysical Research Letters, 34* (5).

Preusker, R., Institut für Weltraumwissenschaften, Freie Universitaet Berlin, D-14195 Berlin.

Robock, A. (2000). Volcanic eruptions and climate. *Reviews of Geophysics*, *38*(2), 191-219.

Robock, Alan and Jianping Mao. (1992). Winter warming from large volcanic eruptions. *Geophysical Research Letters*, 19, 2405-2408.

Rose, W. I., Bluth, G. J. S., & Ernst, G. G. J. (2000). Integrating retrievals of volcanic cloud characteristics from satellite remote sensors: A summary. *Philosophical Transactions of the Royal Society of London. Series A: Mathematical, Physical and Engineering Sciences*, *358* (1770), 1585-1606.

Schneider, D. J., Rose, W. I., Coke, L. R., Bluth, G. J., Sprod, I. E., & Krueger, A. J. (1999). Early evolution of a stratospheric volcanic eruption cloud as observed with TOMS and AVHRR. *Journal of Geophysical Research: Atmospheres (1984--2012)*, *104* (D4), 4037-4050.

Schneider, D. P., Ammann, C. M., Otto-Bliesner, B. L., & Kaufman, D. S. (2009). Climate response to large, high-latitude and low-latitude volcanic eruptions in the Community Climate System Model. *Journal of Geophysical Research, 114* (D15).

Sears, T. M., Thomas, G. E., Carboni, E., A. Smith, A. J., & Grainger, R. G. (2013). SO_2 as a possible proxy for volcanic ash in aviation hazard avoidance. *Journal of Geophysical Research: Atmospheres, 118* (11), 5698-5709.

Sigurdsson, H. (2000). *Encyclopedia of Volcanoes*. San Diego: Academic Press.

Theys, N., Campion, R., Clarisse, L., Brenot, H., Van Gent, J., Dils, B., Van Roozendael, M. (2013). Volcanic SO 2 fluxes derived from satellite data: a survey using OMI, GOME-2, IASI and MODIS. *Atmospheric Chemistry and Physics, 13*(12), 5945-5968.

Thomas, H. E., & Prata, A. J. (2011). Sulphur dioxide as a volcanic ash proxy during the April-May 2010 eruption of Eyjafjallajökull volcano, Iceland. *Atmospheric Chemistry and Physics Discussions*, *11*(3), 7757-7780.

Twomey, S. (1977). The influence of pollution on the shortwave albedo of clouds. *Journal of the Atmospheric Sciences*, *34*(7), 1149-1152.

Vernier, J. P., Thomason, L. W., Pommereau, J. P., Bourassa, A., Pelon, J., Garnier, A., Vargas, F. (2011). Major influence of tropical volcanic eruptions on the stratospheric aerosol layer during the last decade. *Geophysical Research Letters, 38*(12).

Watson, I. M., Realmuto, V. J., Rose, W. I., Prata, A. J., Bluth, G. J. S., Gu, Y., Yu, T. (2004). Thermal infrared remote sensing of volcanic emissions using the Moderate Resolution Imaging Spectroradiometer. *Journal of Volcanology and Geothermal Research, 135*(1-2), 75-89.